Monthly Notices
of the
ROYAL ASTRONOMICAL SOCIETY

MNRAS **444,** 3427–3445 (2014) doi:10.1093/mnras/stu570

The ATLAS^{3D} Project – XXVIII. Dynamically driven star formation suppression in early-type galaxies

Timothy A. Davis,[1⋆] Lisa M. Young,[2,3] Alison F. Crocker,[4] Martin Bureau,[5] Leo Blitz,[6] Katherine Alatalo,[7] Eric Emsellem,[1,8] Thorsten Naab,[9] Estelle Bayet,[5] Maxime Bois,[10] Frédéric Bournaud,[11] Michele Cappellari,[5] Roger L. Davies,[5] P. T. de Zeeuw,[1,12] Pierre-Alain Duc,[11] Sadegh Khochfar,[13] Davor Krajnović,[14] Harald Kuntschner,[15] Richard M. McDermid,[16] Raffaella Morganti,[17,18] Tom Oosterloo,[17,18] Marc Sarzi,[19] Nicholas Scott,[20] Paolo Serra[17,21] and Anne-Marie Weijmans[22]

Affiliations are listed at the end of the paper

Accepted 2014 March 19. Received 2014 March 18; in original form 2013 December 18

ABSTRACT

We present measurements of the star formation rate (SFR) in the early-type galaxies (ETGs) of the ATLAS^{3D} sample, based on *Wide-field Infrared Survey Explorer* (*WISE*) 22 μm and *Galaxy Evolution Explorer* far-ultraviolet emission. We combine these with gas masses estimated from ^{12}CO and H I data in order to investigate the star formation efficiency (SFE) in a larger sample of ETGs than previously available. We first recalibrate (based on *WISE* data) the relation between old stellar populations (traced at K_s band) and 22 μm luminosity, allowing us to remove the contribution of 22 μm emission from circumstellar dust. We then go on to investigate the position of ETGs on the Kennicutt–Schmidt (KS) relation. Molecular gas-rich ETGs have comparable star formation surface densities to normal spiral galaxy centres, but they lie systematically offset from the KS relation, having lower SFEs by a factor of ≈2.5 (in agreement with other authors). This effect is driven by galaxies where a substantial fraction of the molecular material is in the rising part of the rotation curve, and shear is high. We show here for the first time that although the number of stars formed per unit gas mass per unit time is lower in ETGs, it seems that the amount of stars formed per free-fall time is approximately constant. The scatter around this dynamical relation still correlates with galaxy properties such as the shape of the potential in the inner regions. This leads us to suggest that dynamical properties (such as shear or the global stability of the gas) may be important second parameters that regulate star formation and cause much of the scatter around star formation relations.

Key words: stars: mass-loss – ISM: molecules – galaxies: elliptical and lenticular, cD – galaxies: ISM.

1 INTRODUCTION

Star formation (SF) is a fundamental process, responsible for converting the soup of primordial elements present after the big bang into the Universe we see around us today. Despite this, debate still rages about the way SF proceeds, and the role (if any) that environment plays in its regulation. For instance, high-redshift starbursts seem to convert gas into stars much more efficiently than local disc galaxies (Daddi et al. 2010; Genzel et al. 2010). This increased efficiency may be explained by a change in gas properties (e.g. the high fraction of gas at high volume densities in starbursts), or may be an artefact of the imperfect methods we have of estimating star formation rates (SFRs), and tracing molecular hydrogen (Genzel et al. 2012).

Atomic gas is present in ≈32 per cent of early-type galaxies (ETGs; Bottinelli & Gouguenheim 1977; Knapp, Turner & Cunniffe 1985; Morganti et al. 2006; di Serego Alighieri et al. 2007; Grossi et al. 2009; Oosterloo et al. 2010; Serra et al. 2012), dust in ≈60 per cent (Colbert, Mulchaey & Zabludoff 2001; Smith et al. 2012; Agius et al. 2013), and molecular gas in 22 per cent (Combes, Young & Bureau 2007; Welch, Sage & Young 2010; Young et al. 2011, hereafter Paper IV). Low-level residual SF has also been detected through studies of ultraviolet (UV) emission (e.g. Yi et al. 2005; Kaviraj et al. 2007; Salim & Rich 2010; Wei et al. 2010),

⋆ E-mail: tdavis@eso.org

optical emission lines (e.g. Crocker et al. 2011) and infrared emission (e.g. Knapp et al. 1989; Combes et al. 2007; Temi, Brighenti & Mathews 2009, hereafter T09; Shapiro et al. 2010).

Typically ETGs have much smaller fraction of molecular gas to stellar mass than spirals. This average fraction appears to decrease with increasing galaxy bulge fraction (Cappellari et al. 2013b, hereafter Paper XX; see also Saintonge et al. 2012). This suggests a connection between bulge formation and galaxy quenching, as also suggested by optical studies (Bell et al. 2012). However the decrease of the molecular gas fraction does not seem to be the only factor making ETGs red. In fact, even at fixed gas fraction, molecule-rich ETGs form stars less efficiently than normal spirals, and very much less efficiently than high-redshift starburst galaxies (Saintonge et al. 2011, 2012; Martig et al. 2013, hereafter Paper XXII). Such a suppression would help explain how objects in the red sequence can harbour substantial cold gas reservoirs for a long period of time, without becoming significantly blue. A similar suppression of SF may also be ongoing in the central parts of our own Milky Way (Longmore et al. 2013), suggesting this may be a general process in spheroids and/or dense stellar environments. The physics of whatever process is causing this suppression of SF is, however, unknown. The deep potential wells of these objects could hold gas stable against collapse (dubbed 'morphological quenching'; Martig et al. 2009), or strong tidal fields and streaming motions could pull clouds apart (e.g. Kruijssen et al. 2013; Meidt et al. 2013), lowering the observed star formation efficiency (SFE).

In this work we use data from the ATLAS^{3D} project to investigate if local ETGs do display a lower SFE than local spirals, and if so what may be driving this suppression. ATLAS^{3D} is a complete, volume-limited exploration of local (<42 mpc) ETGs (Cappellari et al. 2011a, hereafter Paper I). All 260 ATLAS^{3D} sample galaxies have measured total molecular gas masses (or upper limits; from Institut de Radioastronomie Millimétrique (IRAM) 30 m CO observations presented in Paper IV). H I masses are also available for the northern targets (from Westerbork Synthesis Radio Telescope, WSRT, observations; Serra et al. 2012, hereafter Paper XIII). To estimate the SFR in these objects, we utilize data from the *Wide-field Infrared Survey Explorer* (*WISE*; Wright et al. 2010) all sky survey at 22 μm, and from the *Galaxy Evolution Explorer* (*GALEX*) in the far-ultraviolet (FUV).

Section 2 presents the data we use in this work, and describes how derived quantities are calculated. Section 3 presents our results, where we investigate the 22 μm emission from CO non-detected ETGs, and the SF activity in objects with a cold interstellar medium (ISM). Section 4 discusses these results, and what we can learn about SF and the evolution of ETGs. Section 5 presents our conclusions.

2 DATA

In this paper we consider the ATLAS^{3D} sample of ETGs. This sample was carefully selected based on morphology to include every early-type object (brighter than −21.5 in K_s band) visible from the William Herschel Telescope, out to a distance of 42 mpc, and is thus a complete, volume-limited sample. More information on the sample selection can be found in Paper I. In this work we consider two subsamples, those galaxies with a detected molecular ISM that can provide fuel for SF (from Paper IV), and those without. Here we consider entire galaxies in an integrated manner. A spatially resolved SF analysis will be presented in a future work. To estimate the SFE in these objects, we require both molecular and atomic gas masses, tracers of obscured and unobscured SF, and sizes for the regions concerned. We describe below how these were obtained.

2.1 Molecular gas masses

The CO(1-0) and CO(2-1) lines were observed in every galaxy in the ATLAS^{3D} sample at the IRAM 30 m telescope, and 56 objects were detected (for full details see Paper IV). From these observations we have estimated molecular gas masses for the detected galaxies, using a Galactic X_{CO} factor of 3×10^{20} cm^{-2} (K km s^{-1})$^{-1}$ (Dickman, Snell & Schloerb 1986). We return to discuss this assumption later, but as ETGs usually have high stellar metallicities such a value is a priori reasonable. Making this assumption, we found molecular gas reservoirs with masses between 10^6 and $10^{9.5}$ M$_\odot$, as tabulated in Paper IV. We were also able to place limits on the amount of molecular gas of CO non-detected objects, finding upper limits between 10^6 and 10^8 M$_\odot$ (for objects at different distances).

These observations were single pointings at the galaxy centres, with a beam size of ≈22 arcsec for the CO(1-0) transition (used to calculate the molecular gas masses). In some objects the molecular gas distribution was later shown to be more extended than the 30 m telescope beam (see Davis et al. 2013a, hereafter Paper XIV, for an analysis of the total molecular gas extent in these objects). In these cases, we use total interferometric CO fluxes from Alatalo et al. (2013, hereafter Paper XVIII). In principle it is possible that these interferometric observations resolved out some emission, which would make our CO masses lower limits. The correction for molecular material outside the beam of our single-dish observations is much more significant, however, and so we consider it better to use the interferometric fluxes where possible. As the CO is not generally extremely extended, we do not expect the amount of flux resolved out to be large, so this should not affect our conclusions. In objects without interferometric observations, we used the single-dish CO fluxes to estimate the masses. Our size estimates (described below) suggest that very few of these unmapped objects have extended gas reservoirs, so these 30 m telescope measurements are unlikely to miss substantial amounts of molecular material.

2.2 Atomic gas masses

As presented in Paper XIII, all ATLAS^{3D} field galaxies above a declination of 10° were observed with the WSRT, with a resolution of ≈35 arcsec. For Virgo cluster objects we take the data from the arecibo legacy fast ALFA (ALFALFA) survey (di Serego Alighieri et al. 2007), as documented in Paper XIII. Most of the molecular discs studied here are smaller than 35 arcsec, so we assume that only the H I gas mass detected in the innermost beam is important. The central H I mass used here is listed in table A1 of Young et al (2011). In many cases the H I in the central regions is unresolved. When calculating the combined gas surface density we assume that the H I is cospatial with the CO. In galaxies with large H I discs (Class 'D' in Paper XIII), we assume that the H I disc has a uniform surface density over the entire inner beam. This is an assumption, but has been shown to be reasonable in other galaxies, where H I emission saturates in the inner parts of the discs (e.g. Wong & Blitz 2002; Bigiel et al. 2008). In objects below a declination of 10°, where we have no H I observations, we assume that the H I mass is negligible. We expect this assumption to be reasonable, given that the other objects we study here are all molecular gas dominated in the inner parts.

2.3 22 μm fluxes

Emission at ≈20–25 μm traces warm dust, that is present around hot newly formed stars, in the ejected circumstellar material around hot old stars, and in active galactic nuclei (AGN) torii. If one can

correct for the emission from old stars (in the absence of strong AGN), the ≈20–25 μm emission can provide a sensitive estimate of the amount of obscured SF in our systems.

Here we use 22 μm fluxes from the *WISE* catalogue (Wright et al. 2010) all sky data release. We chose to use *WISE* 22 μm rather than *Spitzer* 24 μm observations as the *WISE* data are available for every source in our sample, at a reasonably uniform depth (and Ciesla et al. 2014 have shown that where multiple measurements exist the scatter between *Spitzer* 24 μm and *WISE* 22 μm fluxes is low). We downloaded the *WISE* 22 μm catalogue profile fit magnitudes (*w4mpro*) and aperture magnitude values (parameter *w4gmag*) from the *WISE* catalogue (Wright et al. 2010). The aperture values are calculated using elliptical apertures defined from the position, size and inclination of the galaxy from the Two Micron All Sky Survey (2MASS; Skrutskie et al. 2006) Extended Source Catalog (Jarrett et al. 2000), and enlarged by the *WISE* team to correct for the larger point spread function of the *WISE* satellite. See the *WISE* documentation[1] for full details of these magnitudes.

As some of our sources are (marginally) extended compared to the *WISE* beam, and the profile fit magnitudes are known to underestimate the true flux for extended sources, we preferentially use the aperture flux values (parameter *w4gmag*). In CO-detected objects we verified that the apertures used in the catalogue are always larger than the CO distribution. In a few objects (usually the most star-forming objects with compact gas reservoirs) the profile fit magnitudes retrieve more flux, and so we instead use these *w4mpro* values. The 22 μm fluxes we measure for each object (and the respective errors, as listed in the catalogue) are listed in Table 1 for our CO detected sample. For the CO non-detected sample we always use the aperture magnitudes, and list the derived 22 μm luminosities in Table A1. The method we use to calculate SFRs while removing the contribution of old stars is discussed in Sections 3.1 and 3.2.

2.4 FUV fluxes

FUV light is emitted primarily by young O and B stars, and hence traces SF activity over the last ≈0.1 Gyr. In the most massive and old ETGs, the UV-upturn phenomenon is observed, in which additional FUV light is emitted by an older population of stars (likely post-asymptotic giant branch stars; Yi 2008; Bureau et al. 2011). The light from this phenomenon is diffuse, following the old population, and is energetically unimportant if even low-level SF is present (Yi et al. 2005). Thus we do not expect this phenomenon to substantially affect measurements of SF derived from FUV in this work. If it were to have an effect, however, it would formally make our SF estimates upper limits.

FUV magnitudes for the star-forming galaxy sample used in this work were obtained from the *GALEX* catalogue server, release GR7. Where multiple observations of the same target exist, we always used the deepest observation. These magnitudes are corrected for foreground extinction assuming the Milky Way $E(B-V)$ values from Schlegel, Finkbeiner & Davis (1998) scaled to UV using $A_{FUV} = 8.24\ E(B-V)$ (Gil de Paz et al. 2007). The FUV flux measured for each object (and its error) is listed in Table 1. The method used to calculate SFRs is discussed in Section 3.2.

2.5 Source sizes

To estimate the mean surface density of gas and SF tracers, one needs to know the total area over which they are distributed. For most of the objects in our star-forming sample, the area can be directly estimated from the size of the molecular gas reservoir seen in our interferometric CO observations. This size is listed in column 3 of table 1 in Paper XIV.[2] The typical gas reservoir is found to have a radial extent of ≈1 kpc. In Paper XIV we also present a 'beam corrected' size for the CO reservoirs, but as such a process is intrinsically uncertain we here choose to use the observed measured extents (making our adopted sizes formally upper limits). If at our resolution the gas appears to be in a disc, the area is estimated assuming the gas is in a flat circular disc, with a diameter given by the observed major axis length. Where our observations reveal rings of gas (either spatially or in velocity space; see Papers XIV and XVIII), the rings are assumed to have a radial width of 200 pc. This is an assumption based purely on the size of the rings that are visible in optical images in some well-resolved cases (e.g. NGC 4324). If the molecular rings were smaller, the surface density of gas used would be underestimated. The galaxies in which we make this correction are NGC 2685, NGC 2764, NGC 3626, NGC 4324 and NGC 5866.

For those objects where only single-dish molecular gas data exist, we estimate the area of the star-forming regions using resolved images of gas and/or SF tracers. In this work we estimate the size of these regions using the highest resolution tracer available. Where possible we use *Hubble Space Telescope* (*HST*) images of UV emission, or unsharp-masked optical *HST* images that pick out patchy dust (that has been shown to be almost always cospatial with the cold gas, occasionally slightly more extended; Paper XVIII). Where *HST* observations are not available, we use the size of the FUV-emitting region, as estimated from *GALEX* images (resolution ≈6 arcsec), the size of strong Balmer line emitting regions in our SAURON integral field unit observations (resolution ≈1–2 arcsec), or the size of the 24 μm emission in *Spitzer* images (resolution ≈6 arcsec). The source sizes we measure, and the data these are based on, are listed in Table 1. We include the additional uncertainty in size coming from the limited spatial resolution of some of these data, as shown in Table 1. We use these source sizes to estimating the surface densities of both SF and gas tracers.

3 RESULTS

3.1 22 μm emission from CO non-detected ETGs

As discussed above, the hot dust that gives rise to 22 μm emission from galaxies occurs both in the birth clouds around newly formed massive stars and in the circumstellar ejecta of old stars. T09 studied the 24 μm emission of 18 CO non-detected elliptical galaxies from the SAURON galaxy sample (de Zeeuw et al. 2002; a subset of the sample studied here). They found that the 24 μm emission from these objects correlates well with the K_s-band luminosity (a proxy for stellar mass), as would be expected from emission from an old stellar population.

We here reproduce such a correlation in Fig. 1, but using 22 μm *WISE* luminosities for all 260 galaxies of the ATLAS^{3D} sample. Our sample galaxies that contain no detectable molecular ISM are shown as red circles, while molecular gas-rich objects are shown in blue. A typical error bar is shown in the bottom-right corner of the plot. The K_s-band luminosity of each object has been estimated

[1] http://wise2.ipac.caltech.edu/docs/release/allsky/–accessed 30/05/13.

[2] In the published version of Paper XIV the size entries for several galaxies were incorrect. We here use the correct D_{CO} values of 20 arcsec for NGC 4150 and 21.2 arcsec for NGC 4526.

Table 1. Properties of the star-forming ETG sample used in this work.

Galaxy	Area (kpc^2)	Source	$\log \Sigma_{H\,I+H_2}$ ($M_\odot\ pc^{-2}$)	τ_{dyn} (Myr)	τ_{ff}	$F_{22\,\mu m}$ (mJy)	$F_{22\,\mu m,corr}$ (mJy)	F_{FUV} (μJy)	$\Sigma_{SFR,22\,\mu m}$ ($\log M_\odot\ yr^{-1}\ kpc^{-2}$)	$\Sigma_{SFR,FUV+22\,\mu m}$
(1)	(2)	(3)	(4)	(5)	(6)	(7)	(8)	(9)	(10)	(11)
IC0676	2.51 ± 0.83	PXIV	2.31 ± 0.22	66.1	8.1	550.0	545.5 ± 3.7	238 ± 4.1	−0.51 ± 0.19	−0.46 ± 0.18
IC0719	10.31 ± 2.04	PXIV	1.33 ± 0.17	51.5	14.3	58.7	53.9 ± 0.4	652 ± 27.6	−1.68 ± 0.14	−1.76 ± 0.12
IC1024	4.29 ± 1.02	PXIV	2.24 ± 0.19	63.2	8.4	339.1	336.0 ± 1.9	652 ± 8.6	−0.91 ± 0.15	−0.93 ± 0.14
NGC 0509	3.81 ± 1.36	24 μm	0.90 ± 0.23	77.6	18.2	5.7	3.8 ± 0.2	2 ± 0.8	−2.20 ± 0.20	−2.54 ± 0.23
NGC 0524	3.76 ± 0.97	PXIV	1.39 ± 0.19	18.3	13.7	51.5	2.8 ± 1.9	239 ± 7.5	−2.53 ± 0.31	−2.36 ± 0.15
NGC 1222	1.63 ± 0.92	PXIV	3.12 ± 0.31	65.8	5.1	1824.6	1820.9 ± 17.7	2178 ± 17.8	0.30 ± 0.29	0.55 ± 0.29
NGC 1266	0.03 ± 0.01	A11	4.76 ± 0.16	16.8	2.0	734.4	728.9 ± 5.3	22 ± 4.2	1.27 ± 0.11	1.73 ± 0.13
NGC 2685	0.93 ± 0.35	PXIV	1.66 ± 0.23	20.4	11.8	53.3	37.4 ± 0.9	2066 ± 10.3	−1.35 ± 0.21	−1.03 ± 0.20
NGC 2764	8.63 ± 0.33	PXIV	2.46 ± 0.15	119.7	7.4	300.0	295.8 ± 1.8	473 ± 20.4	−0.81 ± 0.10	−0.82 ± 0.08
NGC 2768	1.48 ± 0.57	PXIV	1.47 ± 0.24	12.9	13.1	51.7	−3.9 ± 1.8	377 ± 9.0	–	−1.94 ± 0.20
NGC 2824	7.80 ± 2.44	PXIV	2.03 ± 0.21	37.6	9.5	74.9	71.9 ± 0.4	78 ± 7.4	−1.26 ± 0.18	−1.38 ± 0.17
NGC 3032	4.85 ± 1.01	PXIV	1.82 ± 0.18	56.4	10.7	136.9	132.1 ± 0.5	1124 ± 6.7	−1.33 ± 0.14	−1.37 ± 0.13
NGC 3073	0.97 ± 0.69	FUV	2.15 ± 0.37	35.8	8.9	8.9	7.2 ± 0.1	309 ± 1.3	−1.49 ± 0.36	−1.27 ± 0.35
NGC 3156	4.23 ± 0.96	PXIV	1.04 ± 0.18	64.5	16.8	14.3	9.2 ± 0.3	147 ± 1.7	−2.21 ± 0.15	−2.37 ± 0.13
NGC 3182	5.79 ± 1.76	PXIV	1.66 ± 0.21	39.2	11.8	33.1	27.4 ± 0.3	524 ± 21.2	−1.62 ± 0.18	−1.61 ± 0.17
NGC 3245	0.09 ± 0.01	HST	2.30 ± 0.15	4.3	8.1	184.0	158.5 ± 1.2	173 ± 4.6	0.09 ± 0.10	0.29 ± 0.08
NGC 3489	0.50 ± 0.18	PXIV	1.58 ± 0.22	18.3	12.3	108.0	67.7 ± 1.3	626 ± 13.7	−1.19 ± 0.20	−1.19 ± 0.19
NGC 3599	0.05 ± 0.01	HST	2.71 ± 0.15	8.7	6.4	33.6	31.4 ± 0.3	9 ± 0.9	0.16 ± 0.11	0.36 ± 0.10
NGC 3607	8.14 ± 1.36	PXIV	1.59 ± 0.17	24.2	12.3	105.9	38.5 ± 2.1	707 ± 5.4	−2.00 ± 0.13	−2.09 ± 0.11
NGC 3619	1.60 ± 0.72	PXIV	2.36 ± 0.26	10.0	7.9	45.9	28.1 ± 0.7	687 ± 7.7	−1.46 ± 0.24	−1.37 ± 0.23
NGC 3626	1.51 ± 0.08	PXIV	2.26 ± 0.15	35.8	8.4	166.7	156.4 ± 1.0	–	−0.71 ± 0.10	–
NGC 3665	8.84 ± 2.10	PXIV	2.16 ± 0.19	25.7	8.8	138.9	55.4 ± 1.2	181 ± 12.8	−1.91 ± 0.15	−2.15 ± 0.14
NGC 4036	1.97 ± 0.73	FUV	1.84 ± 0.23	16.3	10.6	60.0	41.6 ± 0.8	256 ± 4.7	−1.11 ± 0.20	−1.13 ± 0.20
NGC 4111	0.49 ± 0.22	HST	1.71 ± 0.26	17.1	11.4	96.7	84.5 ± 1.0	210 ± 3.7	−0.59 ± 0.24	−0.53 ± 0.23
NGC 4119	1.55 ± 0.44	PXIV	1.95 ± 0.20	38.5	10.0	47.2	29.2 ± 1.2	82 ± 11.0	−1.73 ± 0.17	−1.93 ± 0.17
NGC 4150	1.32 ± 0.33	PXIV	1.71 ± 0.19	41.7	11.5	72.7	67.1 ± 0.5	109 ± 2.4	−1.29 ± 0.15	−1.41 ± 0.14
NGC 4203	0.32 ± 0.18	24 μm	2.04 ± 0.31	8.9	9.5	79.9	35.4 ± 1.2	546 ± 12.6	−1.17 ± 0.29	−1.09 ± 0.28
NGC 4283	0.28 ± 0.17	FUV	1.66 ± 0.34	10.5	11.8	10.6	2.2 ± 0.3	72 ± 3.6	−2.03 ± 0.32	−2.01 ± 0.31
NGC 4324	1.92 ± 0.06	PXIV	1.69 ± 0.15	79.8	11.6	46.9	30.5 ± 0.8	405 ± 22.9	−1.76 ± 0.10	−1.84 ± 0.08
NGC 4429	0.98 ± 0.35	PXIV	2.40 ± 0.23	11.9	7.7	190.2	123.1 ± 5.1	464 ± 28.8	−0.98 ± 0.20	−0.99 ± 0.19
NGC 4435	0.57 ± 0.27	PXIV	2.30 ± 0.27	8.1	8.2	111.9	69.5 ± 2.7	209 ± 4.7	−0.98 ± 0.25	−1.01 ± 0.24
NGC 4459	1.91 ± 0.48	PXIV	1.96 ± 0.19	11.4	9.9	142.3	97.0 ± 2.2	418 ± 6.9	−1.29 ± 0.15	−1.36 ± 0.14
NGC 4476	2.65 ± 0.61	PXIV	1.63 ± 0.18	36.5	12.0	30.3	23.3 ± 0.2	149 ± 4.5	−1.93 ± 0.15	−2.13 ± 0.14
NGC 4477	0.28 ± 0.19	PXIV	2.10 ± 0.36	5.6	9.2	44.6	10.6 ± 1.5	408 ± 7.2	−1.35 ± 0.34	−1.13 ± 0.33
NGC 4526	2.22 ± 0.52	PXIV	2.24 ± 0.18	14.9	8.4	349.9	261.4 ± 8.4	658 ± 7.0	−1.00 ± 0.15	−1.04 ± 0.14
NGC 4596	1.10 ± 0.37	24 μm	1.27 ± 0.22	0.8	14.7	39.8	4.2 ± 1.9	330 ± 6.5	−2.21 ± 0.25	−1.98 ± 0.18
NGC 4643	0.85 ± 0.33	FUV	1.34 ± 0.24	0.7	14.1	87.6	48.9 ± 1.6	31 ± 8.9	−1.25 ± 0.21	−1.37 ± 0.24
NGC 4684	0.38 ± 0.17	FUV	1.63 ± 0.26	22.8	12.0	247.7	238.0 ± 1.0	977 ± 9.5	−0.41 ± 0.24	−0.29 ± 0.23
NGC 4694	1.00 ± 0.35	PXIV	2.06 ± 0.22	73.0	9.3	112.0	97.9 ± 0.8	778 ± 8.7	−1.23 ± 0.20	−1.24 ± 0.19
NGC 4710	2.97 ± 0.07	PXIV	2.61 ± 0.15	91.5	6.8	416.1	383.9 ± 4.6	108 ± 15.7	−0.96 ± 0.10	−1.03 ± 0.10
NGC 4753	4.76 ± 1.07	PXIV	2.02 ± 0.18	33.4	9.6	250.5	110.3 ± 4.3	100 ± 7.6	−1.57 ± 0.15	−1.76 ± 0.14
NGC 5173	4.58 ± 1.76	FUV	2.04 ± 0.24	41.1	9.5	18.1	8.5 ± 0.2	518 ± 6.9	−2.23 ± 0.21	−2.09 ± 0.20
NGC 5273	0.85 ± 0.32	24 μm	1.38 ± 0.23	21.7	13.8	83.9	81.7 ± 0.5	161 ± 3.5	−0.48 ± 0.21	−0.40 ± 0.20
NGC 5379	4.85 ± 1.43	FUV	1.84 ± 0.20	131.2	10.6	39.3	30.0 ± 0.3	245 ± 13.9	−2.05 ± 0.17	−2.26 ± 0.16
NGC 5866	2.39 ± 0.05	PXIV	2.38 ± 0.15	58.7	7.8	225.7	210.5 ± 1.4	495 ± 7.8	−0.67 ± 0.10	−0.64 ± 0.08
NGC 6014	3.71 ± 1.53	PXIV	2.20 ± 0.25	19.1	8.6	130.0	105.1 ± 0.7	430 ± 18.7	−1.57 ± 0.22	−1.72 ± 0.21
NGC 6798	0.69 ± 0.55	FUV	2.45 ± 0.41	13.4	7.5	14.5	8.2 ± 0.3	17 ± 6.6	−1.23 ± 0.40	−1.33 ± 0.43
NGC 7465	10.42 ± 2.04	PXIV	2.15 ± 0.17	64.0	8.9	313.3	310.2 ± 1.8	–	−0.88 ± 0.14	–
PGC016060	1.22 ± 0.04	Hβ	2.18 ± 0.15	25.3	8.8	23.2	18.8 ± 0.2	–	−1.31 ± 0.10	–
PGC029321	3.91 ± 1.73	PXIV	2.02 ± 0.26	45.1	9.6	342.6	341.7 ± 2.5	–	−0.47 ± 0.23	–
PGC056772	0.97 ± 0.83	FUV	2.21 ± 0.44	28.2	8.6	124.2	122.7 ± 0.6	37 ± 6.2	−0.36 ± 0.43	−0.28 ± 0.43
PGC058114	1.12 ± 0.55	PXIV	2.70 ± 0.28	1.8	6.5	504.8	502.3 ± 3.0	115 ± 13.2	−0.26 ± 0.26	−0.16 ± 0.25
PGC061468	5.19 ± 1.75	Hβ	1.28 ± 0.22	57.4	14.6	15.3	14.2 ± 0.2	–	−1.78 ± 0.19	–
UGC05408	1.26 ± 0.43	PXIV	2.53 ± 0.22	34.9	7.2	218.0	216.9 ± 1.0	878 ± 9.7	−0.17 ± 0.19	0.01 ± 0.18
UGC06176	1.87 ± 0.47	PXIV	2.64 ± 0.19	10.2	6.7	232.7	230.3 ± 1.4	–	−0.36 ± 0.15	–
UGC09519	2.52 ± 0.98	PXIV	2.41 ± 0.24	25.0	7.7	30.4	27.5 ± 0.2	–	−1.45 ± 0.21	–

Notes. Column 1 lists the name of the galaxy. Column 2 contains the area of the star-forming region, estimated from the source listed in column 3. PXIV refers to table 1 of Paper XIV, A11 refers to Alatalo et al. (2011), Hβ refers to a size calculated from the Balmer line emitting region visible in SAURON observations. Column 5 lists the total gas surface density derived from the H_2 and H I masses of these objects, as described in the text. Column 5 lists the dynamical time at the outer edge of the molecular disc, calculated from the circular velocity of these galaxies at this radius (see Davis et al. 2011a; Paper XIV). Column 6 contains the local free-fall time of the gas, calculated as in equation (6). Column 7 contains the observed *WISE* integrated 22 μm flux density of the object, before correction for circumstellar emission. Column 8 contains the *WISE* integrated 22 μm flux density corrected for circumstellar emission using equations (1) and (2). Column 9 contains the integrated FUV flux density of the object, after correction for Galactic extinction (Schlegel et al. 1998). A dash in this column indicates that no measurements are available. Column 10 contains the logarithm of the SFR surface density estimated using the equation in Calzetti et al. (2007), after correction for circumstellar emission. Column 11 contains the logarithm of the SFR surface density estimated from corrected 22 μm fluxes and *GALEX* FUV photometry, using the relation from Hao et al. (2011).

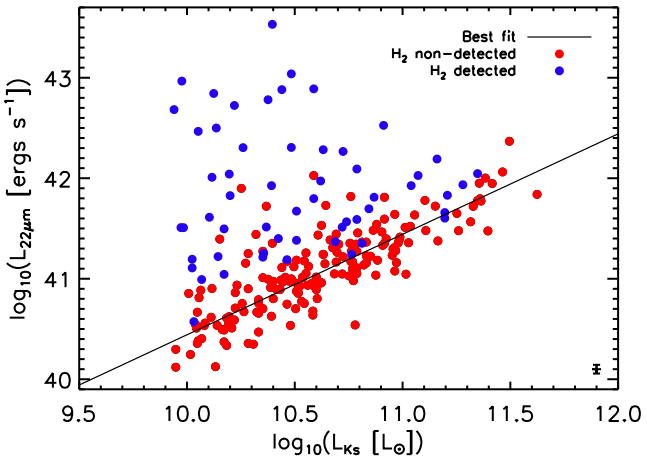

Figure 1. 22 μm *WISE* luminosities of the ATLAS^{3D} galaxies plotted against their K_s-band luminosities. The blue circles are galaxies with detected molecular gas and the red circles are those ETGs without a detected molecular ISM. The best fit to the ATLAS^{3D} galaxies without a detected molecular ISM is shown as a black solid line. The typical error on each point is shown in the bottom-right corner of the plot.

from its 2MASS K_s-band magnitude, assuming that the absolute magnitude of the Sun at K_s band is 3.28 mag (table 2.1 of Binney & Merrifield 1998). To be consistent with the other papers in this series, we use the $K_{s,total}$ magnitude (parameter k_m_ext from the 2MASS catalogue; Jarrett et al. 2000; Skrutskie et al. 2006), as tabulated in Paper I. These $K_{s,total}$ magnitudes are measured over large apertures, to include the total flux from the galaxy using the techniques developed in Kron (1980) and curves of growth (see Jarrett et al. 2000 for further details). Distances to these galaxies are given in Paper I. The *WISE* and 2MASS luminosities we derived for the sample objects are listed in Table A1.

Our CO non-detected galaxy sample shows a clear correlation with galaxy luminosity, but with a significant scatter. Galaxies with molecular gas show no clear correlation between their 22 μm emission and stellar luminosity, but always lie above the mean location of the CO non-detected galaxies for any given stellar luminosity, strengthening our suspicion that the bulk of their 22 μm emission is SF related. Some galaxies in our CO non-detected sample (≈10 per cent) also lie well above the relation formed by the majority of the CO non-detections. Some of these galaxies lie systematically at the edge of our survey volume, where our molecular gas detection limit is highest, and are thus likely star-forming systems which lie below our CO detection limit. Others have young stellar population ages in their central parts (suggesting they may have been star forming in the recent past) or have active AGN. We discuss these objects in more detail in Fig. 2 and below.

We conduct a robust fit (using the LTS_LINEFIT[3] routine described in Cappellari et al. 2013a; hereafter Paper XV) to determine the mean amount of 22 μm emission caused by old stellar populations at each stellar mass. The coefficients of the best-fitting relation are shown in equation (1), and the systems that were considered outliers are indicated with a cross in Table A1. We note that doing a simple fit including all the outliers (that are likely star forming) would slightly change the slope of the derived relation, but would not alter our conclusions,

$$\log\left(\frac{L_{22\,\mu m,passive}}{\mathrm{ergs\,s^{-1}}}\right) = (1.00 \pm 0.04)\log\left(\frac{L_{K_s}}{\mathrm{L_\odot}}\right) + (30.45 \pm 0.46). \quad (1)$$

In order to estimate the amount of 22 μm emission arising exclusively from SF in our CO detected sample, we subtract off the contribution of the passive stellar populations (following T09):

$$L_{22\,\mu m,SF} = L_{22\,\mu m,obs} - L_{22\,\mu m,passive}, \quad (2)$$

where $L_{22\,\mu m,passive}$ is obtained from the $K_{s,total}$ luminosity via equation (1).

For CO non-detected galaxies, the scatter around the best-fitting relation in Fig. 1 is large (≈0.4 dex), larger than the expected uncertainty in either luminosity. We searched for an astrophysical explanation for this intrinsic scatter. Galaxies with no detected molecular ISM that have large H I discs, clouds or disturbed H I distributions do not show any enhancement in 22 μm emission over and above that expected for a passive population. Galaxies with small H I discs do lie above our best-fitting relation for CO non-detected objects, consistent with having some small but non-negligible contribution from SF at 22 μm, but as only two cases are present in our sample these objects do not drive the intrinsic scatter observed.

When controlling for stellar luminosity, the offsets above and below the line defined in equation (1) for the CO non-detected sample do not correlate with stellar kinematic quantities (Emsellem et al. 2011; Krajnović et al. 2011), ionized-gas quantities, or measures of galaxy environment (Cappellari et al. 2011b). Stellar population age (or equivalently the strength of Hβ absorption; McDermid et al., in preparation) does show a weak trend (Fig. 2, left-hand panel), in that the systems with the youngest (<4 Gyr) mean stellar populations (detected in any aperture) tend to lie above the best-fitting relation (likely due to a larger number of asymptotic giant branch (AGB) stars, that are important sources of dust creation from a stellar population). However the vast majority of galaxies in our CO non-detected sample are dominated by older stellar populations, and the residuals around equation (1) do not correlate with age beyond 4 Gyr. Mathews et al. (2013) found that the metallicity of the stellar population is an important driver of the scatter in this relation at fixed mass. With a larger sample of objects we are unable to reproduce this trend (Fig. 2, centre panel).

Our CO non-detected galaxy sample does not contain many strong AGN, but lower luminosity nuclear activity could contribute to the scatter seen in Fig. 1 (as the torus region of an AGN emits in the mid-infrared; e.g. Rujopakarn et al. 2010). The 31 galaxies in our CO non-detected sample that have radio cores in the Faint Images of the Radio Sky at Twenty-Centimetres (FIRST) survey (Becker, White & Helfand 1995) do tend to lie above our best-fitting relation (see Fig. 2, right-hand panel). Removing galaxies with radio cores does not substantially affect our best fit (equation 1). Almost all the X-ray-bright AGN identified in our sample (by Sarzi et al. 2013) also have a molecular ISM, so they do not contribute to the scatter discussed here. The presence of central ionized-gas velocity dispersion peaks often correlates with low-level nuclear activity (Sarzi et al., in preparation), but we do not see any clear trend in the residuals of galaxies with such an enhancement.

3.2 Star formation rates

Many different conversions exist to convert an observed flux in a given waveband to an SFR. These are primarily empirical

[3] Available at http://www-astro.physics.ox.ac.uk/

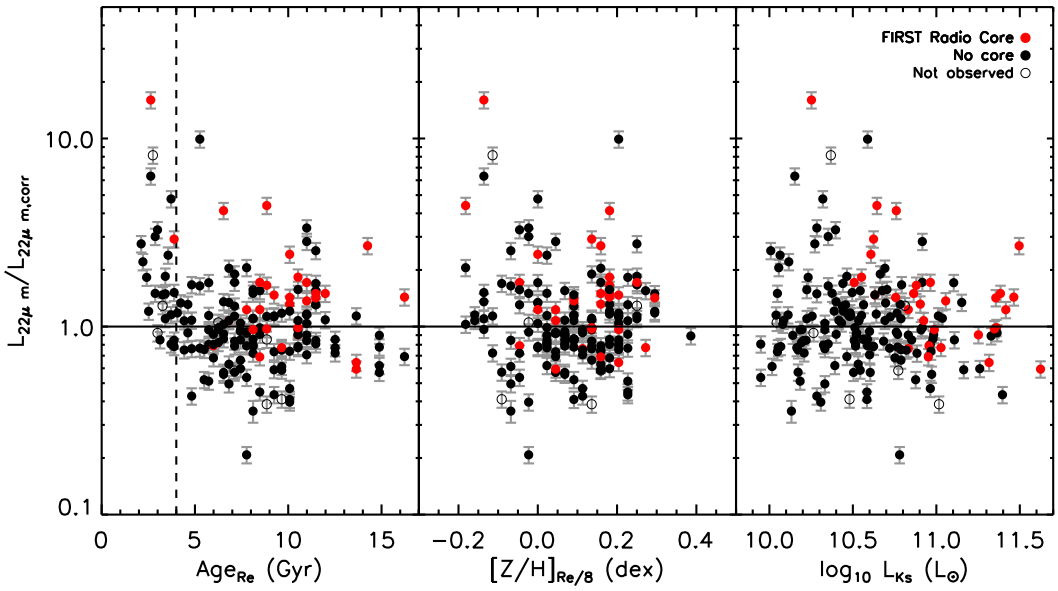

Figure 2. Residuals around the best-fitting line from Fig. 1 plotted as a function of galaxy properties, for the CO non-detected ATLAS^{3D} ETGs. The left-hand panel shows residuals versus the age of the stellar population in the galaxy, measured within a one effective radius aperture. The vertical dashed line in this panel is a guide to the eye at a population age of 4 Gyr (as discussed in the text). In the centre panel the residuals are plotted as a function of the central metallicity of the galaxy (measured in an Re/8 aperture; using aperture values with one effective radius would not change our conclusions). The right-hand panel shows the residuals against the K_s-band luminosity of the galaxy, as measured for Fig. 1. The solid black line is our best-fitting relation from Fig. 1. The red circles denote galaxies which have a compact radio core, and the black circles those without. The open circles show objects that are not in the FIRST survey volume.

conversions, often based on observations of nearby galaxies. Consistency between SFR estimates made using different tracers is thus only likely if the conversions are calibrated against the same set of sample galaxies. Here we use the results of Calzetti et al. (2007) to estimate SFRs from our measured 22 μm fluxes. We also use a combined relation from Hao et al. (2011) to estimate the SFR from *WISE* and *GALEX* data together. This combined relation extinction corrects the *GALEX* fluxes, using the total infrared to FUV luminosity ratio (IRX) method. This extinction correction is very important, as without it FUV SFRs can be underestimated by half an order of magnitude (see Hao et al. 2011 for full details). This allows us to estimate the contribution from both obscured and unobscured SF (based on a Kroupa initial mass function, IMF, burst of age 1 Gyr). Both of these calibrations are formally for 24 μm *Spitzer* observations, but the bandpasses of the *Spitzer* 24 μm and *WISE* 22 μm filters (and the spectral energy distributions of galaxies in this region) are sufficiently similar that the error induced by using *WISE* 22 μm measurements should be minimal. Importantly, the SF calibrations we use are both based on the *Spitzer* Infrared Nearby Galaxies Survey, and thus should be internally consistent. Using an SFR estimator derived specifically for *WISE* 22 μm data but not calibrated on the same galaxy sample, such as that by Shi et al. (2012), would not change the conclusions of this paper.

When using 22 μm fluxes in either of these two conversions considered we first remove the emission from the passive old stellar populations (using equations 1 and 2, as discussed above). One CO-detected object falls below the correlation in equations (1) and (2) (NGC 2768), suggesting it has low amounts of obscured SF, and thus the 22 μm band is dominated by emission from old stellar populations. We remove this object from our analysis of 22 μm SFRs from this point on, but do include this object in the combined 22 μm + FUV relations, by assuming that its 22 μm flux is zero (and hence all the SF is unobscured).

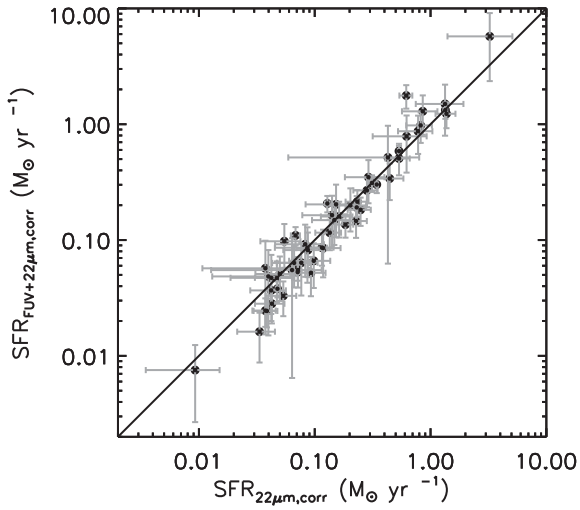

Figure 3. Comparison of SFRs derived using *WISE* 22 μm emission only, and *WISE* 22 μm combined with *GALEX* FUV emission for our star-forming galaxy sample. The solid line shows the 1:1 relation to guide the eye.

For each galaxy in our star-forming sample, we list both SFRs we estimate in Table 1. The errors in these SFRs are estimated through propagation of the uncertainties in the input quantities, and these are also listed in Table 1. The SFRs estimated from the 22 μm emission alone agree well within the errors with those estimated from FUV emission combined with 22 μm emission (see Fig. 3). The ratio of the SFRs derived with and without the FUV does not show any correlation with galaxy mass, confirming that the UV-upturn phenomenon is not adversely affecting the UV-derived SFRs. The ratio of these two SFRs may weakly depend on the SFR

itself (the best-fitting relation with a fixed intercept between these two indicators has a slope of 1.03±0.02), but more data would be needed to confirm if this low significance trend is real. Overall, the agreement between these SFRs suggests that ETGs have ratios of obscured and unobscured SF similar to those of spiral galaxies.

3.2.1 Literature comparison

As part of the ATLAS^{3D} survey, we have also estimated SFRs in some of these objects from *Spitzer* observations of (non-stellar) 8 μm emission (Falcón-Barroso et al., in preparation; including the earlier results of Shapiro et al. 2010).

23 of our molecular gas-rich samples have *Spitzer* measurements. The scatter between the 8 and 22 μm measures of SF is larger than that between the two 22 μm-based measures discussed above, but generally the agreement is good, with a scatter of ≈0.4 dex. The 8 μm SFRs were estimated using the calibration of Wu et al. (2005), that is based upon a different galaxy sample, and this may be the cause of the larger scatter.

3.3 Kennicutt–Schmidt relations

SF relations are usually given with respect to SFR and gas surface densities, i.e. $\Sigma_{\rm SFR} \propto \Sigma^{n}_{\rm H\,I+H2}$, where n is some power-law exponent. This is physically motivated by theoretical predictions that SF depends on gas volume density (e.g. Schmidt 1959), and additionally removes the distance dependence of the relation. For a sample of local star-forming spiral and starburst galaxies, (Kennicutt 1998, hereafter K98) found $n = 1.4$ (the so-called Kennicutt–Schmidt, KS, relation), as shown below after correction to a Kroupa (2001) IMF:

$$\log_{10}(\Sigma_{\rm SFR}) = (1.4 \pm 0.15)\log_{10}\left(\Sigma_{\rm H\,I+H_2}\right) - (3.76 \pm 0.12), \quad (3)$$

where $\Sigma_{\rm SFR}$ is in units of $\rm M_\odot\,yr^{-1}\,kpc^{-2}$ and $\Sigma_{\rm H\,I+H_2}$ is in units of $\rm M_\odot\,pc^{-2}$. A value of n greater than unity implies that the SFE (where SFE $\equiv$ SFR/$M_{\rm gas}$) increases in high column density clouds. Other works studying SF within spatially resolved regions in nearby spiral galaxies suggest a constant SFE (i.e. $n \approx 1$; Young & Scoville 1991; Young et al. 1996; Bigiel et al. 2008). We compare our ETGs to both the KS relation and the constant SFE relation of Bigiel et al. (2008, hereafter B08) in Figs 4 and B1.

In addition to the controversy surrounding the slope of the KS relation, it seems that high-redshift starburst galaxies form more stars per unit gas mass than their local analogues (e.g. Daddi et al. 2010; Genzel et al. 2010, hereafter D10+G10). This has led to the suggestion that two different SF regimes exist: a long-lasting mode for discs (evolving secularly) and a more rapid mode for rapidly star-forming high-redshift objects (with major mergers and/or dense SF regions). We investigate where our sample of ETGs falls with respect to these two SF modes in this section.

Fig. 4 shows the surface density of SF (derived using 22 μm emission only in the top row of panels, and the combined FUV+22 μm calibration in the bottom row), plotted against the surface density of $\rm H_2$ and H I in our $\rm H_2$-rich galaxy sample (calculated as described in Section 2). We do not show plots with the molecular gas only, as these objects are molecule dominated and hence the derived SF relations are almost identical. The plots in the left-hand column show all our samples of $\rm H_2$-rich ETGs, while the plots in the right-hand column show only those objects where CO interferometry is available, leading to a better determination of the total CO flux and directly measured molecular gas reservoir sizes. Fig. 4 also shows the SF relation of K98 as a blue line, with the 1σ error region shaded in grey. The best fit to our data points is shown as a solid red line, while the best fit with a slope fixed to that found by K98 is shown as a dashed red line. The coefficients of these fits are shown in the figure legends, and are reproduced in Table 2. Fig. B1 is analogous to Fig. 4, with the constant SFE relation of B08 shown for comparison (rather than K98).

Fig. 5 shows our ETGs and the spiral and starburst galaxies of K98 on the same plot for comparison. We show only the galaxies from this work with CO interferometry available, and use SFRs derived from the combination of *WISE* and *GALEX* data. We also include the ETGs from Paper XXII, where we have spatially resolved SFRs (in radial bins) for six of our sample ETGs, calculated from non-stellar 8 μm emission. Our trend based on global measurements agrees well with the resolved observations presented in that paper (although the best-fitting slope to the PXXII sample would be slightly shallower).

Although generally within the scatter of the original K98 relation, it is clear for all indicators that our ETGs have a lower average SFE than both the spiral and starburst galaxies making up the sample of K98 (and thus a much lower SFE than the high-redshift objects of D10+G10). The left-hand column of plots in Fig. 4 (which includes all objects) shows increased scatter, as expected given the larger uncertainties on the reservoir areas and masses, but they still suggest that the SFE of ETGs is lower than that of later type objects. The zero-points of the best-fitting relations with a fixed slope (listed in Table 2) suggest a relation offset by a factor of between 2.2 and 2.5 from that of K98 (depending on the tracer/sample selection), and a factor of ≈17 from that of the high-redshift starbursts. These mean offsets are significant at greater than a 3σ level, even given the large scatter in the observations. Looking at the galaxies individually, it is clear that this effect is dominated by a specific set of objects, whose properties will be discussed further below.

The slopes of our best-fitting relations when using only 22 μm as a tracer of SF are slightly shallower than the relation of K98, with slopes of $n = 1.19\pm0.03$ and 1.11 ± 0.04 (when fitting all galaxies and those with interferometric data only, respectively). These are still steeper than a constant SFE relation, as can clearly be seen in Fig. B1. When using a calibration with both FUV and 22 μm fluxes our best fits are steeper, with $n = 1.49\pm0.04$ and 1.31 ± 0.04, respectively, consistent with the slope found by K98. B08 suggest that when one investigates SF in a spatially resolved fashion (rather than in an integrated manner as done here), one obtains a shallower relation. The slope obtained with resolved observations in Paper XXII is indeed shallower (as seen in Fig. 5). However, this result is still the subject of some debate (e.g. Momose et al. 2013), and we will investigate this matter further when presenting spatially resolved SF relations for all these galaxies in a future work.

3.4 Elmegreen–Silk relation

An alternative parametrization of the relation between SFR and gas surface density depends on the dynamical time at the edge of the star-forming gas disc ($\tau_{\rm dyn}$), as shown below (Elmegreen 1997; Silk 1997):

$$\Sigma_{\rm SFR} \propto (\Sigma_{\rm H\,I+H2/\tau_{dyn}})^{n}. \quad (4)$$

K98 also placed their sample of spiral and starburst galaxies on this relation (estimating the radial extent of the gas by finding the edge of the main Hα or Brγ-emitting disc). They found a tight linear correlation, that is an equally good description of the data points as

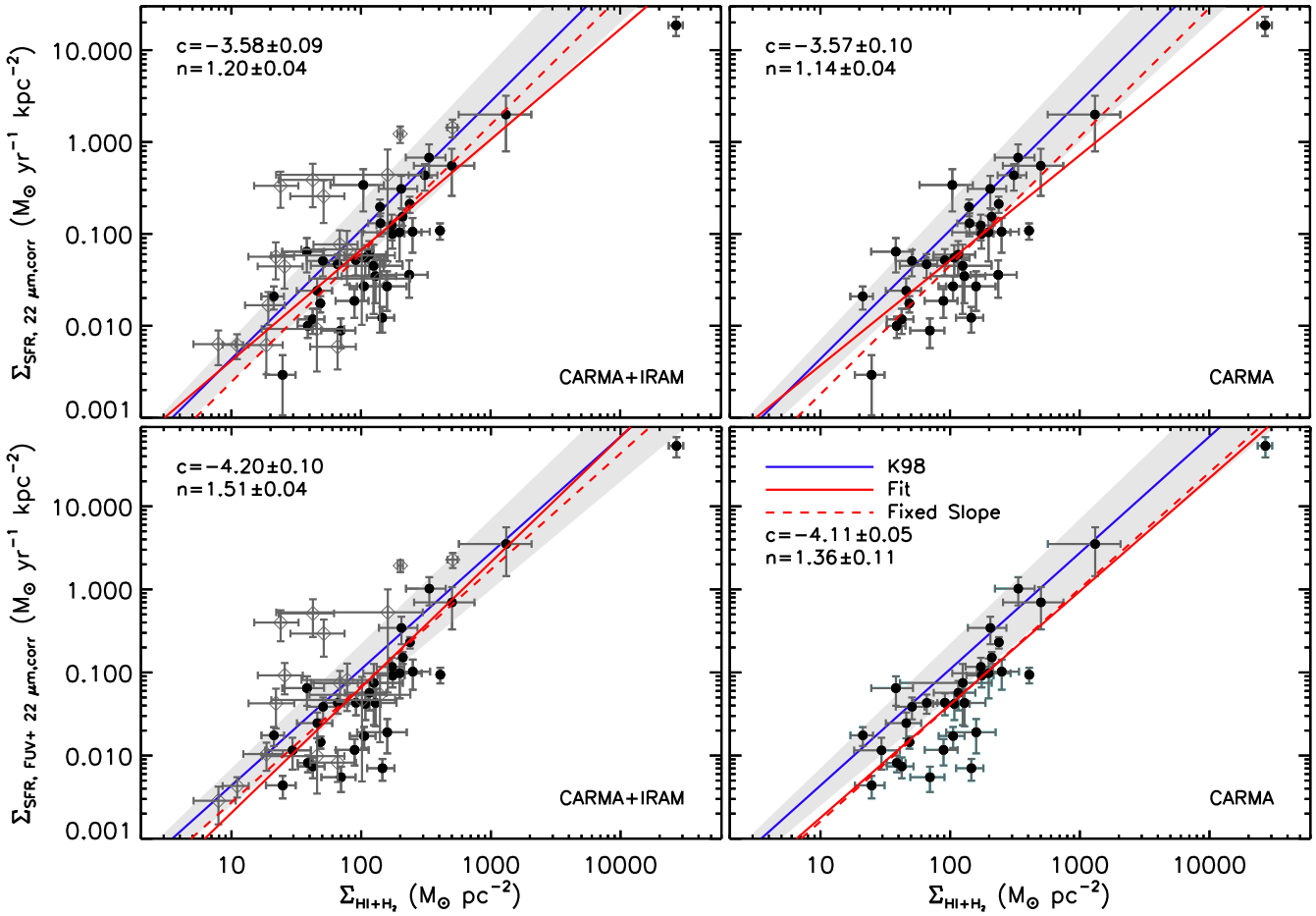

Figure 4. The SFR surface density of molecular gas-rich ATLAS^{3D} ETGs, shown as a function of the gas (atomic and molecular) surface density. The $H_2 + H\,I$ surface densities are estimated as described in Section 2, and the SFRs as described in Section 3.2. The data points have had the fraction of their 22 μm emission arising from circumstellar emission removed, as described in Section 3.1. The top row shows SFR densities derived from *WISE* data only, while the bottom row shows SFRs derived from a combination of *GALEX* FUV and *WISE* 22 μm emission. The black circles denote galaxies where resolved interferometry is available from Paper XVIII (allowing better estimates of the total molecular gas mass and density) and the open symbols show galaxies for which only IRAM 30 m telescope data are available. The left-hand column shows all galaxies, while in the right-hand column the IRAM points have been removed to include only our most reliably determined data points. The galaxy which appears at the top right of every panel is NGC 1266, which hosts a large molecular gas outflow (see Alatalo et al. 2011; Davis et al. 2012 for more details). We show in all panels the K98 SF relation (for local spiral/starburst galaxies) converted to a Kroupa IMF as a solid blue line, with its typical scatter indicated as a grey shaded area. Our best-fitting SF relations for ETGs are shown as red solid and dashed lines, for the relation with a free and fixed slope, respectively. The legend of each plot indicates the fitted slope and intercept of the best unconstrained fit.

equation (3). Their best-fitting relation is (again after correction to a Kroupa IMF):

$$\frac{\Sigma_{\rm SFR}}{\rm M_\odot\,yr^{-1}\,pc^{-2}} = 0.106 \left(\frac{\Sigma_{\rm H\,I+H_2}}{\rm M_\odot\,pc^{-2}}\right) \left(\frac{\tau_{\rm dyn}}{\rm yr}\right)^{-1}, \quad (5)$$

We estimate the dynamical times of our sample galaxies using the ATLAS^{3D} mass models from Paper XV, from which we can extract a circular velocity ($V_{\rm circ}$) profile as a function of radius, assuming a mass-follows-light model (models A of Paper XV). Although our galaxies contain dark matter, as well as stellar matter, this contributes only 13 per cent in median within R_e, which is generally larger than the region where we detect CO. This implies that the total mass profile has a slope very close to that of the stellar distribution alone, justifying our use of mass-follows-light models. We define the dynamical time at the outer edge of the gas disc (as determined in Paper XIV) simply as $\tau_{\rm dyn} = 2\pi R/V_{\rm circ}$. The dynamical times for our objects are listed in Table 1. Paper XIV has shown that the molecular gas is dynamically cold and follows well the circular velocity profile in the majority of our objects, and hence this $\tau_{\rm dyn}$ measurement should provide good estimates of the dynamical times within the molecular gas itself.

Fig. 6 shows the position of our molecular gas-rich sample ETGs (red circles) with respect to the Elmegreen–Silk (E-S) relation of K98 (as in equation 5). Also plotted for comparison are the spiral (black circles) and starburst (blue circles) sample of K98.

Our ETGs fall systematically below the E-S relation, with a large scatter. The best fit to our sample (assuming the same linear slope as K98) is $\Sigma_{\rm SFR} = 2.96 \times 10^{-3} \Sigma_{\rm gas} \Omega_{\rm gas}$, suggesting ETGs turn ≈2 per cent of their gas into stars per dynamical time, a factor of ≈6 lower than spiral/starburst galaxies (and high-redshift starbursts which are also found to obey the E-S relation; e.g. D10+G10). The ETGs fall in the gap between the spiral galaxies and starburst nuclei on this plot, in the same region as spiral galaxy centres (as shown in K98), but they are offset to lower SFRs. The cause of this effect will be discussed further in Section 4.4.

Table 2. KS relation fits.

SF indicator	Sample	n	c	$\chi^2_{\rm red}$
			$\log(M_\odot\ yr^{-1}\ kpc^{-2})$	
(1)	(2)	(3)	(4)	(5)
22 μm	All	1.20 ± 0.04	-3.58 ± 0.09	6.74
22 μm	All	1.40	-4.01 ± 0.02	7.12
22 μm	PXVIII	1.14 ± 0.04	-3.57 ± 0.10	3.83
22 μm	PXVIII	1.40	-4.15 ± 0.03	4.66
FUV + 22 μm	All	1.51 ± 0.04	-4.20 ± 0.10	9.90
FUV + 22 μm	All	1.40	-3.96 ± 0.02	10.02
FUV + 22 μm	PXVIII	1.36 ± 0.05	-4.11 ± 0.11	4.23
FUV + 22 μm	PXVIII	1.40	-4.19 ± 0.03	4.25

Notes. This table contains the fitted slope and intercept for the KS relations presented in Fig. 4 (here parametrized as $\log_{10}(\Sigma_{\rm SFR}) = n \log_{10}(\Sigma_{\rm gas}) + c$). Column 1 lists the SFR indicator used, and column 2 the sample of galaxies included in the fit. PXVIII refers to the interferometrically mapped sample of Paper XVIII. The slope (n) and intercept (c) of the best fits are given in columns 3 and 4. Where the slope was fixed to $n = 1.4$ (the best-fitting value of K98), this is indicated in column 3 and no error bar is reported on the slope. Column 5 shows the reduced χ^2 for each fit, indicating how well the best-fitting values represent the observed data points.

3.5 Local volumetric SF relations

An alternative approach to unifying SF relations is to assume that SFE is set by the local value of the gas free-fall time. As discussed in depth in Krumholz, Dekel & McKee (2012, hereafter KDM12), such a volumetric SF relation can reproduce observations of both Galactic and extragalactic star-forming sources. The local free-fall time that is relevant for SF can be calculated in several ways, depending on whether the ISM of the object is assumed to be in small bound units (such as giant molecular clouds; GMCs) or a continuous sheet with local density variations. The former is thought to be a more physical model of low-redshift galaxies, while the latter is thought to be appropriate in high-redshift and starbursting sources.

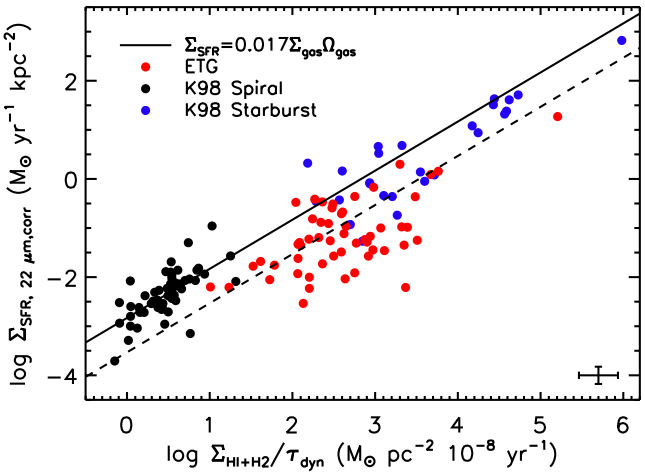

Figure 6. As the top-right panel of Fig. 2, but with the gas surface densities divided by the dynamical time (estimated at the outer edge of the molecular gas disc). Only galaxies with interferometic CO maps available are included. Molecular gas-rich ATLAS^{3D} ETGs are the red circles, while the spiral and starburst objects of K98 are shown in black and red, respectively. The best fit reported in K98 is shown as a black line, and the best fit to our points, assuming the same slope as K98, is shown as a dashed line. The intercept of the best-fitting line corresponds to ETGs turning ≈2 per cent of their gas into stars per dynamical time, a factor of ≈5 lower than spiral/starburst galaxies. The mean error bar on the ETG data points is shown in the bottom-right corner.

The fundamental parameters that vary in the GMC based free-fall time ($t_{\rm ff,GMC}$) estimates are the gas velocity dispersion and the observed gas density (see equation 6 below). No study of the molecular gas velocity dispersion in ETGs currently exist, but Davis et al., in preparation, suggest that this dispersion is low, and likely similar to local spirals which have $\sigma_{\rm gas} \lesssim 12\ {\rm km\ s^{-1}}$ (Caldu-Primo et al. 2013). Assuming this velocity dispersion does not strongly vary between sources, the GMC based estimate of free-fall time just depends on

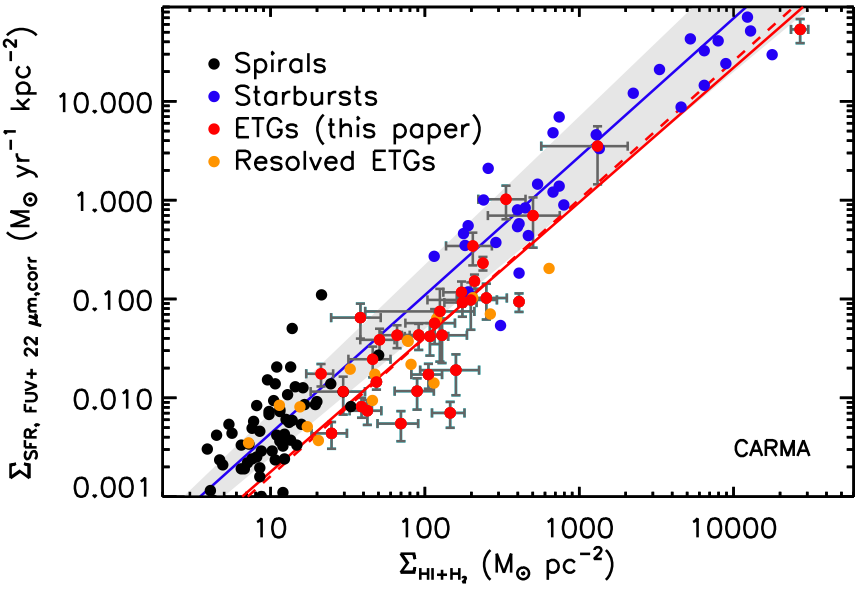

Figure 5. As the bottom-right panel of Fig. 4, but showing for reference the spiral and starburst objects of K98 (where the SFRs were calculated from Hα emission, and have been corrected to a Kroupa IMF) and the spatially resolved SFRs (in radial bins) of six ETGs (presented in Paper XXII, where the SFR was calculated from non-stellar 8 μm emission).

the gas surface density itself (making this correction factor a simple rotation of the points in log space)

$$t_{\rm ff,GMC} = \frac{\pi^{\frac{1}{4}}}{\sqrt{8}} \frac{\sigma_{\rm gas}}{G(\overline{\Sigma_{\rm GMC}}^{3}\,\Sigma_{\rm gas})^{\frac{1}{4}}}, \quad (6)$$

where G is the gravitational constant, $\sigma_{\rm gas}$ is the gas velocity dispersion (assumed here to be a constant 8 km s^{-1} as in KDM12), $\Sigma_{\rm gas}$ is the observed (galaxy average) gas surface density and $\overline{\Sigma_{\rm GMC}}$ is the average GMC surface density, which we here assume is a constant 85 m$_\odot$ pc^{-2}, as in KDM12.

The alternative (starburst) prescription from KDM12 assumes that SF is regulated by the dynamical stability of a continuous disc of gas, that globally should have a Toomre Q parameter (Toomre 1964) of ≈1. In this case the parameters needed to calculate the free-fall time are the dynamical time (which enters the equation linearly), and the logarithmic derivative of the rotation curve ($\beta = \frac{\delta \ln(V)}{\delta \ln(R)}$) which enters to the power of −0.5. In objects where the majority of the gas reaches beyond the turnover of the galactic rotation curve $\beta \approx 0$, and the free fall time simply depends on the dynamical time (as in the E-S SF relation discussed in Section 3.4).

We calculate the local free-fall times for our ETGs using the relations of KDM12. We find that the GMC estimate (the functional form of which is shown in equation 6) is shorter in all objects, and hence dominant. This is expected, as local ETGs are usually not starbursts, and have been observed to have most of their molecular mass in discreet GMCs (Davis et al. 2013c). The adopted free-fall times are listed in column 5 of Table 1.

Using the free-fall time calculated from equation (6), in Fig. 7 we plot our ETGs on the local volumetric SF relation of KDM12. Also plotted for comparison are the spiral (black circles) and starburst sample (blue circles) from K98 (with free-fall times as calculated by KDM12). Our ETGs fall on to the relation of KDM12, suggesting that on average they convert ≈1 per cent of their gas into stars per *local free-fall time*. We discuss this result further in Section 4.4.

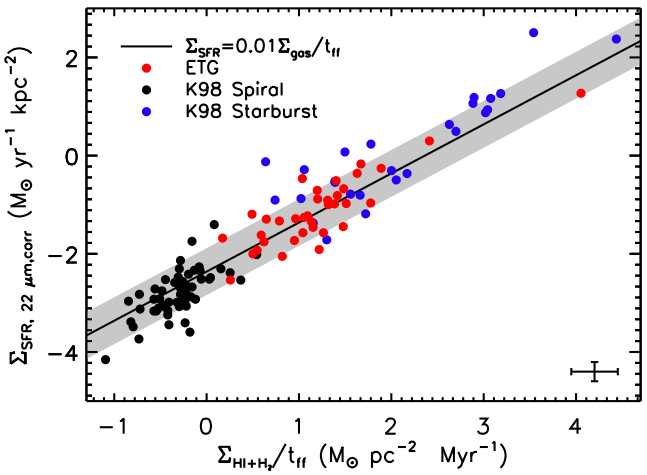

Figure 7. As the top-right panel of Fig. 2, but with the gas surface densities divided by the local free-fall time (estimated using equation 6). Only galaxies with interferometic CO maps available are included. Our ATLAS^{3D} ETGs are the red circles, while the spiral and starburst objects of K98 (with free-fall times as calculated in KDM12) are shown in black and red, respectively. The best fit reported in KDM12 is shown as a solid black line. It provides a good fit to our ETGs, so we do not plot our own fitted relation. The mean error bar on the ETG data points is shown in the bottom-right corner.

3.6 Dynamical drivers of star formation suppression

The fact that local ETGs do not follow the same relationship between SF and gas surface density in Fig. 4 suggests that there is some difference in the way SF proceeds in these objects. Fig. 7 suggests this may be a dynamical effect, as only when accounting for the relevant local time-scale is a universal SF relation obtained, where molecule-rich ETGs form the same fraction of stars per free-fall time as nearby spiral and starbursting objects. The obvious difference between ETGs and local spiral galaxies is that they tend to have, deeper, steeper potential wells. In this section we investigate if the shape of the potential correlates with the suppression of SF discussed above.

In Fig. 8 (panel a) we plot the gas depletion time (≡M$_{\rm gas}$/SFR = 1/SFE) for those sample galaxies which were mapped in Paper XVIII, against the extent of the molecular gas (tabulated in Paper XIV) normalized by the location of the turnover in the rotation curve of that object (estimated from the JAM model circular velocity profiles published in Paper XV, as in Davis et al. 2011a; Paper XIV). Fig. 8 shows that galaxies with long depletion times (and thus low SFE) have the majority of their molecular gas confined within regions where the rotation curve of the galaxy is still rising. The rest of the objects, which have more of their gas within the flat part of the galaxy rotation curve, have depletion times and SFEs consistent with those found for normal spiral galaxies (≈0.5–1.5 Gyr).

We also plot in Fig. 8, panel (a) a simple mixing model (shown as a dashed line). This toy model assumes that two SF regimes exist within ETGs, one with very low SFE (which is valid in the rising part of the rotation curve), and one with a normal SFE, similar to that found in local spirals (which is valid in the flat part of the galaxy rotation curve). We assume depletion times of 0.8 Gyr for the normal regime, and a Hubble time for the low SFE regime, respectively. We then assume that all the gas is distributed in an exponential disc (which is only true for ≈50 per cent of these sources; Paper XIV), and that the maximum gas extent we can measure corresponds to three scalelengths. We then vary the scalelength of this disc with respect to the turnover of rotation curve, and calculate a model 'integrated' depletion time by weighting the two assumed depletion times by the fraction of gas in each regime. This leads to the curve shown in Fig. 8. This toy model is likely to be a vast oversimplification, and the exact values of all the assumed parameters were simply selected to provide a by-eye fit to the data. Despite this, the functional form produced by such a toy model reasonably matches the behaviour seen in the data, suggesting that the suppression of SF we observe may be driven by the fraction of gas which is inside the turnover radius.

In panel (b) of Fig. 8 we plot the gas depletion time against the fraction of the molecular gas mass that lies within the turnover of the rotation curve ($\frac{M(r<R_{\rm peak})}{M_{\rm tot}}$). We calculate this using the resolved CO maps from Paper XVIII, laying down an elliptical aperture at the turnover radius (with ellipticity calculated using the inclinations of these objects from Paper V; Davis et al. 2011a), and determining the fraction of the CO flux coming from inside this radius. Despite the limited resolution of our CO maps causing significant scatter, this panel broadly confirms our interpretation of panel (a), showing that systems with the majority of their molecular gas mass lying within the turnover of the galaxy rotation curve have longer depletion times. The dashed line is a guide to eye fitted to the black points, and has the form

$$\log(T_{\rm dep}) = (0.73 \pm 0.11)\frac{M(r < R_{\rm peak})}{M_{\rm tot}} - (0.20 \pm 0.08). \quad (7)$$

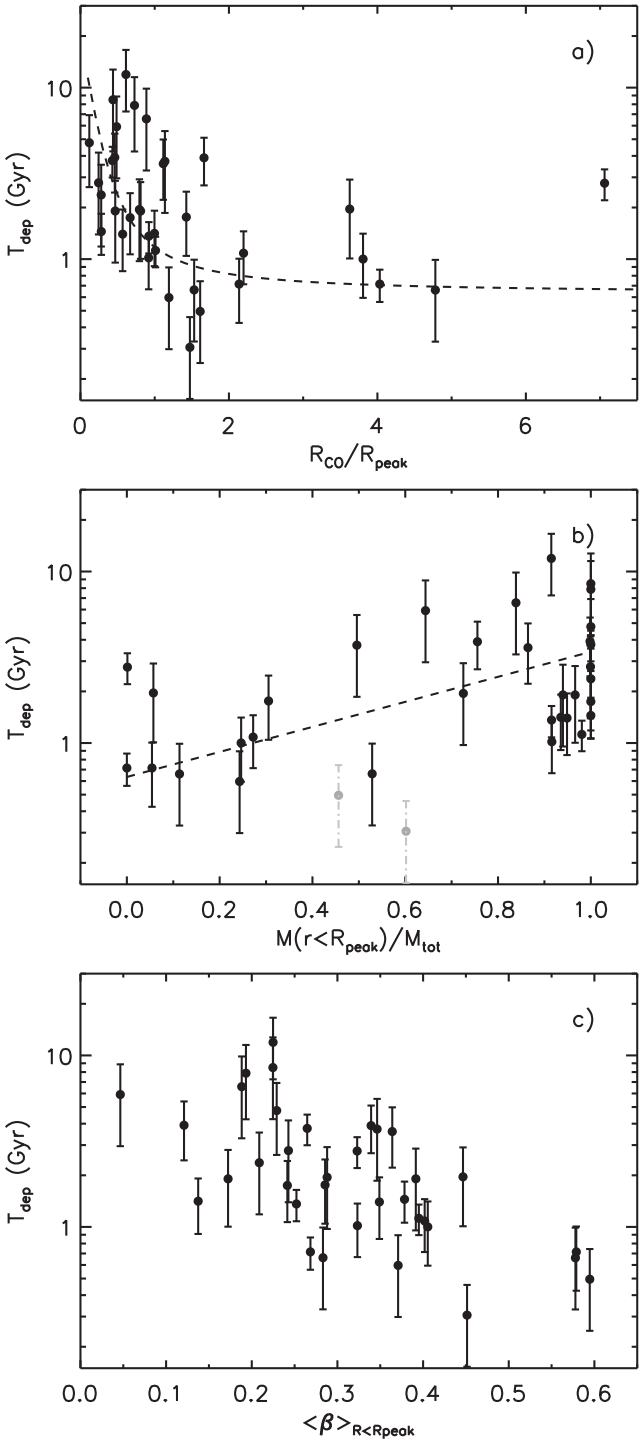

Figure 8. Gas depletion times plotted in panel (a) as a function of the extent of the molecular gas, normalized by the location of the turnover in the galaxy rotation curve. The dashed line shows a simple mixing model as described in the text, where gas depletion times are assumed to be a Hubble time in the rising part of the rotation curve, and ≈0.8 Gyr in the flat part. Panel (b) shows the fraction of the molecular gas mass present inside the turnover radius. The grey points are galaxies where within our beam size we cannot determine this quantity accurately. The dashed line is a guide to eye fitted to the solid points. Panel (c) shows the mean logarithmic derivative of the rotation curve in the inner part of the rotation curve (inside R_{peak}).

In panel (c) of Fig. 8 we plot the depletion time against the logarithmic derivative of the rotation curve (β; as defined in Section 3.5), a variable in defining the stability of the gas disc (see KDM12). We average this quantity over the inner portion of the galaxy, where the rotation curve is rising, as this is the area that seems to be involved in SF suppression (see panels a and b). This variable describes how steeply rising the rotation curve is, with value of zero being expected for a flat rotation curve, and value of 1 representing solid body rotation. Fig. 8, panel (c) shows that these variables anticorrelate, although with reasonable scatter (Spearmans rank correlation coefficient of −0.6). On average it seems that galaxies with the strongest suppression of SF have fast rising rotation curves, which plateau before reaching the peak velocity, leading to β values as low as ≈0.1. Galaxies with more normal depletion times, on the other hand, have rotation curves that rise more steadily to a peak, with average values of $\beta \approx 0.35$.

Following directly from panel (c), it should be noted that the shear rate (A/Ω) is directly related to the derivate of the galaxy rotation curve, as

$$\frac{A}{\Omega} = -0.5\left(\frac{1}{\Omega}\frac{\mathrm{d}V}{\mathrm{d}R} - 1\right), \quad (8)$$

where A is the first Oort constant, Ω is the angular velocity ($\propto V/R$), V is the circular velocity, and R is the radius. Thus the depletion time would positively correlate with the mean shear rate in the inner regions. Thus it seems that galaxies which do not form stars efficiently have higher shear rates than those with more normal SFEs. It is not clear if shear can really be the only factor governing the SFE in ETGs however, as A/Ω is even higher in the flat part of these galaxies rotation curves, where the SFE appears to be normal.

4 DISCUSSION

4.1 22 μm emission from old stars

In Fig. 1 we explored the relationship between 22 μm emission and K_s-band luminosity in CO non-detected ETGs. A strong relationship was confirmed between K_s-band magnitude and 22 μm emission (as presented in T09), however the amount of emission from CO non-detected galaxies can vary by almost half an order of magnitude between objects of the same mass. AGN activity and galaxies with young stellar populations (<4 Gyr) contribute to this scatter, but they do not dominate it. This poses interesting questions about the nature of this emission, and of the scatter, in molecule poor galaxies.

It has been suggested that this mid-infrared emission comes from circumstellar material around (post-) asymptotic giant branch (AGB) stars (Athey et al. 2002). All stars between 0.8 and 8 $m_\odot$ will go through an AGB stage (Herwig 2005), but from a single burst of SF the number of stars going through this (relatively short-lived) phase is a strong function of time. Additionally, the dust production rate from AGB stars is thought to scale with luminosity, so higher mass AGB stars (that die quickly) produce more dust than their lower mass counterparts (Boyer et al. 2012). As massive ETGs have harsh radiation fields, dust would be expected to be destroyed (through sputtering) on short time-scales ($\lesssim$46 myr; Clemens et al. 2010) if no cold ISM is available to shield it, so a constant supply of new dust is required. Overall we would expect that galaxies that have not formed many new stars in the last 12 Gyr should not have as many AGB stars (per unit luminosity, or mass), and thus not as much 22 μm emission as relatively young galaxies. As also found by Temi, Brighenti & Mathews (2005), there seems to be no relation

between the amount of 22 μm emitting dust and stellar population age beyond 4 Gyr, and hence perhaps another source of dust may be important in old galaxies.

Many other potential dust production mechanisms (such as supernovae; e.g. Matsuura et al. 2011) should also be strongly linked to the stellar population age, and so cannot explain neither the dust emission observed in these old galaxies, nor the residuals about the best-fitting relation in Fig. 1. Mergers could bring in new dust (and new stars that produce dust), but they cannot explain the smooth distribution of this dust throughout these (gas poor) galaxies (Athey et al. 2002), and the strong link between the stellar luminosity of the galaxy and the warm dust emission. Mergers could potentially contribute to the scatter seen at fixed galaxy luminosity seen in Fig. 1, but given the short lifetime of dust in these objects, the merger rate would have to be high.

Perhaps emission from very small grains (VSGs; Sellgren 1984) could help explain dust emission from these old passive galaxies. VSGs seem to have a longer lifetime in the ISM (Hirashita 2010), and are produced during the destruction of larger crystalline dust grains. The intrinsic scatter around the best-fitting relation in Fig. 1 remains largely not understood, however a full exploration of this phenomenon is beyond the scope of this paper.

4.2 Star formation rates

For this sample of molecular gas-rich ETGs we find SFRs between ≈0.01 and 3 $m_\odot$ yr^{-1}, and SFR surface densities ranging from ≈0.004 to 18.75 $m_\odot$ yr^{-1} kpc^{-2}. The median SFR for our molecular gas-rich ETGs is ≈0.15 $m_\odot$ yr^{-1}, and the median SF surface density is 0.06 $m_\odot$ yr^{-1} kpc^{-2}. We find that almost all molecule rich ETGs have higher SFR surface densities than average spiral galaxies. They lie in the same region of the KS plot (Fig. 4) as the spiral galaxy centres from K98. This may be a selection effect, as galaxies with widespread SF would likely not have been morphologically classified as early type, and our flux-limited CO survey biases us to objects with high molecular gas surface brightness. A deeper survey would be required to determine if some ETGs have low surface density discs like those found in spirals, or if such objects are truly absent.

Overall it is clear that simply selecting ETGs (by either colour or morphology) is not a good way to ensure that a galaxy sample is free from SF activity, as is often assumed by studies at higher redshifts.

4.3 Star formation relations and efficiencies

Fig. 4 clearly shows that ETGs, on average, form a factor of ≈2.5 fewer stars per unit molecular gas mass than late-type and starburst galaxies (and a factor of ≈20 fewer than high-redshift starbursts).

Our estimate of a lower SFE by a factor of ≈2.5 agrees well with the decrease of SFE observed for galaxies with redder colours, higher stellar mass concentrations, and/or higher stellar mass densities in the COLD-GASS survey (Saintonge et al. 2011, 2012), and (for a subsample of eight of the objects studied here) in the resolved SF study published in Paper XXII. This factor of 2 also is similar to predictions from simulations of gas in idealized galaxies which is affected by 'morphological quenching' (Martig et al. 2009; Paper XXII).

It is clear that ETGs do not fit well in a picture where the SFE is assumed to be constant (B08), or even in a bimodal theory with star bursting and regular SF modes. Instead, as we show above that the SFE varies smoothly as a function of galaxy properties, a likely more physical model would be that a continuum of SF modes exist, spanning the range between extreme high SFE starbursts and our low efficiency early-type objects.

In our study, this difference is mainly driven by galaxies with SFRs below ≈0.3 $m_\odot$ yr^{-1} kpc^{-2} (or equivalently cold gas surface densities <300 $m_\odot$ pc^{-2}). The few systems above this limit are consistent, within their errors, with following a standard KS relation (and lie above the constant SFE relation of B08 in Fig. B1). These systems generally have dense circumnuclear gas reservoirs, and would likely be considered as central starbursts if located in a late-type galaxy.

The systems with the lowest SFEs all have cold gas surface densities of around ≈100 $m_\odot$ pc^{-2}. These systems tend to have extended molecular gas discs, that appear to be dynamically relaxed and follow exponential molecular gas surface brightness profiles (Paper XIV), but have the majority of their gas situated in the rising part of the galaxy rotation curve (see Section 3.6). We below consider if the offset observed in these systems could be caused by changing gas properties, or the difficulty of estimating SFRs and molecular gas masses.

4.3.1 *Difficulties in estimating star formation rates*

SFRs are notoriously difficult to calibrate. They rely intimately on knowing the number of massive stars formed in a given SF episode, and thus the number of ionizing photons. The SFR calibrations we used here have all been calibrated in normal star-forming spiral/starburst galaxies. However, the physical conditions within our ETGs may be different in ways that violate the assumptions made in these calibrations. For instance, if the dust properties (e.g. size distribution or composition) were different in ETGs, then our 22 μm fluxes could be systematically higher or lower than expected.

The formation of dust is a controversial subject, but it is thought that stellar winds from AGB/pAGB stars are likely to be important (e.g. Ferrarotti & Gail 2006). As ETGs tend to be metal rich and have large α-element enhancements, the dust formed in the mass-loss of such stars could be different from that found in late-type objects. If dust is accreted from external sources, of course, then that complicates matters further (Clemens et al. 2010, Davis et al. 2011b, hereafter Paper X). Additionally, all SFR calibrations make assumptions about the SF history of the objects (usually that the SFR has been constant over the past ≈100 myr to 1 Gyr). In our ETGs, where much of the gas may have been accreted recently, a much more bursty SF history may be more applicable.

Recent evidence has suggested that the IMF is unlikely to be universal (e.g. van Dokkum & Conroy 2010; Cappellari et al. 2012), and varies as a function of galaxy properties. In particular in Paper XX we found the mass normalization of the IMF to be related to the bulge fraction, which is also correlated to galaxy quenching. We have assumed here a Kroupa IMF for every object, but any object-to-object variation that depends on galaxy or ISM physical properties could affect the SF relation retrieved. Our objects are present in the sample of Cappellari et al. (2012), however, and we do not see any clear trend between the SFE and the IMF.

Another factor that can affect our SFR determination is the interstellar radiation field (ISRF). In the spiral/starbursting systems where our SFR relations are calibrated, the ISRF is dominated by irradiation from newly formed OB stars. It is this light that we see directly in the FUV, and re-radiated in the infrared. In ETGs, however, various population of old stars generate intense hard radiation fields, that can dominate the ionization structure of the ISM (Sarzi et al. 2010). The most massive ETG systems also host large X-ray

haloes, that provide an additional source of heating. We note however that in general these processes would increase the fluxes of the radiation we are using to trace SF, and would thus make us overestimate the SFR in these galaxies. This can therefore not remove the discrepancy present in Fig. 4, where our calculated SFRs are low by a factor of ≈2.5.

4.3.2 *A changing* X_{CO}

The molecular gas surface densities used here assume a Galactic X_{CO} factor (the conversion between CO flux and H_2). X_{CO} has been shown to vary as a function of metallicity (e.g. Wilson 1995; Bolatto et al. 2008; Leroy et al. 2011; Sandstrom et al. 2012) and in high-redshift starbursts (e.g. Solomon et al. 1997; Downes & Solomon 1998). Other observational evidence from local starbursts (Hinz & Rieke 2006; Meier et al. 2010), the Galactic Centre (Oka et al. 1998) and high-z submillimetre galaxies (Tacconi et al. 2008) suggest that X_{CO} may also be lower in regions of high molecular surface density. See Bolatto, Wolfire & Leroy (2013) for a review of this issue.

Our objects are generally metal rich (with metallicities around solar or above), where X_{CO} changes little. Thus including the effect of a varying X_{CO} with metallicity would change little the SFE of our ETGs. We also find no correlation between the SFE of our objects and stellar metallicity (although it is possible that the gas-phase metallicity is different, if gas has been accreted; Paper X). The objects that show the largest SFE suppression in our data also do not have particularly dense molecular gas reservoirs, when compared to other systems where density driven X_{CO} variations have been observed.

As part of the BIMA-SONG survey, Regan et al. (2001) showed that molecular gas embedded in the bulges of spiral galaxies seems to emit more strongly (in the CO(1-0) line) than gas in the disc regions. Sandstrom et al. (2012) suggest that this may be due to a changing X_{CO}, possibly caused by the higher ISM pressure within a large bulge. However, Leroy et al. (2013) found that SF in spiral galaxy centres is more efficient than normal even when taking into account a variable X_{CO}, the opposite of the effect observed here. By construction our systems are even more bulge-dominated than the objects studied by Leroy et al. (2013), and thus the effects of a changing X_{CO} could be stronger. The galaxies with the strongest observed SF suppression also have the majority of their gas in the central regions of the galaxy, where they would be most susceptible to this issue.

Overall we are unable to rule out the possibly that a lower X_{CO} in individual objects could be contributing to the scatter in the relations we observe. However, we find it unlikely that X_{CO} is lower in all objects uniformly, as then our ETGs would no longer lie on the KDM12 relation (as presented in Fig. 7) instead lying above it on average, forming more stars per unit mass and free-fall time.

4.3.3 *Changing gas properties*

If the gas reservoirs in the objects that have low SFEs were to be substantially different from those found in other galaxies, this could help explain the discrepancy. For instance, if shear and/or bulge pressure increased the amount of low density CO emitting gas, this could cause us to overestimate molecular gas masses (see Section 4.3.2 above). Equally, if the fraction of dense gas were lower than normal in these objects, this could reduce the number of stars that are able to form.

To search for signs of such changes in molecular gas properties, we correlated the SFE of our molecular gas-rich ETGs with the molecular gas line ratios presented for some of these objects in Krips et al. (2010), Crocker et al. (2012) and Davis et al. (2013b). Some of these objects with molecular line ratio information have low SFE, while others are consistent with having the same SFE as spiral galaxies. The $^{12}CO/^{13}CO$ ratio is usually assumed to be an indicator of the mean optical depth of the CO emitting gas. If the amount of low density gas in these systems is increasing due to dynamical/pressure effects, one might expect the objects with low SF efficiencies to have smaller mean optical depths. We find however that the $^{12}CO/^{13}CO$ ratio does not correlate with the SFE in these objects, and (as shown by Crocker et al. 2012) the $^{12}CO/^{13}CO$ ratios in these objects are similar to those usually found in spiral galaxies.

In a similar way, if the dense gas fraction is lower in objects with suppressed SF then we would expect the ratio of dense gas tracers (such as HCN, HCO^+ and CS) to CO isotope emission to be suppressed. We find here that the HCN/CO, HCO^+/CO and CS/CO ratios do not correlate with the SFE, and again are in the normal range found for spiral galaxies. This suggests that the properties of the molecular clouds in these galaxies are not different in any systematic way that could explain the observed SFE suppression. This is backed up by the analysis in Bayet et al. (2013) and Davis et al. (2013b), who found that the gas in these ETGs has similar physical properties (density, temperature) to gas in normal spiral galaxies and the Milky Way.

4.4 Dynamically regulated star formation

In Section 4.3 we discussed the possibility that the low SFE we observe in these objects could be an artefact of changing gas properties, or the difficulty of estimating SFRs and molecular gas masses. We find no evidence that definitively points to such a solution for this discrepancy. Indeed, one of the strongest arguments against such solutions are that they do not adequately explain the systematic behaviour of the SFE as a function of galaxy dynamics. In this section we discuss the possibility that these dynamical effects play a dominant role in regulating SF in this sample of fast-rotating ETGs.

We showed above that one can obtain a single SF relation that fits ETGs, low- and high-redshift spiral/starburst galaxies and galactic clouds, if you normalize the gas density by the local free-fall time, as shown in Fig. 7. Our ETGs are constant with using up ≈1 per cent of their gas per local free-fall time, and the scatter around this relation is reasonably low.

Despite this, Fig. C1 in Appendix shows that once again, additional parameters correlate with the scatter seen around the KDM12 relation. The shape of the potential (β) and relative gas extent all correlate with the ratio of the depletion time to the free-fall time. If the gas velocity dispersion, or average cloud mass, which we have assumed to be constant, change systematically with these properties then this could lead to these dependences.

We briefly discussed above the possible importance of shear. Shear induced by galactic rotation acts to prevent gravitational collapse of gas clouds, which will increase the Jeans mass required for them to become bound, potentially influencing the mean cloud density (Toomre 1964). In addition, strong shear that pulls clouds apart, or an increased presence of hot gas in galaxy centres could increase gas velocity dispersions. A similar correlation between shear and specific SFR has been found in the discs of some spiral galaxies (Seigar 2005), suggesting this process may be important (however, it should be mentioned that shear appears to matter little in Milky Way star-forming regions and some spiral objects; Dib et al. 2012; Meidt et al. 2013).

KDM12 also present an alternative prescription for calculating the free-fall time, that assumes that SF is regulated by the dynamical stability of a continuous disc of gas, which globally should have a Toomre Q parameter (Toomre 1964) of $\approx$1. In this case dynamical time and β enter the equation for free-fall time directly. In Fig. C1 we do not use this formalism, as GMC time-scales dominate, but the remaining correlations with these parameters suggest that the global stability of the disc could still be important.

5 CONCLUSIONS

In this paper we presented SFRs for the (fast-rotating) molecule-rich ATLAS^{3D} ETGs, derived from *WISE* 22 μm and *GALEX* FUV data. We first recalibrated the relation between K_s-band luminosity and 22 μm emission for our large sample of CO non-detected ETGs, to allow subtraction of 22 μm emission from circumstellar material around old stars. The emission from CO non-detected galaxies can vary by almost half an order of magnitude between objects of the same stellar mass. AGN activity and galaxies with younger stellar populations (<4 Gyr) contribute to this scatter, but do not dominate it. We were unable to reproduce claimed correlations between stellar metallicity and the scatter in this relation, and thus the astrophysical driver of the majority of the scatter remains unknown.

Once the contribution from old stars has been removed, we found SFRs between $\approx$0.01 and 3 $m_\odot$ yr^{-1}, and SFR surface densities ranging from $\approx$0.004 to 18.75 $m_\odot$ yr^{-1} kpc^{-2}. The median SFR for our molecular gas-rich ETGs is $\approx$0.15 $m_\odot$ yr^{-1}, and the median SFR surface density is 0.06 $m_\odot$ yr^{-1} kpc^{-2}. Almost all molecule-rich ETGs have higher SFR surface densities than the disc of the average spiral galaxy, but similar to spiral galaxy centres. This is depute many of the galaxies being bulge dominated, and lying in the red sequence on an optical colour–magnitude diagram. It is thus clear that selecting early-type objects by morphology or optical colour is not a good way to build a sample free from SF activity, as is often assumed by studies at higher redshifts.

Using these SFRs, we showed that our ETGs fall below the canonical KS relation, forming on average a factor of $\approx$2.5 fewer stars per unit molecular gas mass than late-type and starburst galaxies (and a factor of $\approx$20 fewer than high-redshift starbursts). In our study, this difference is mainly driven by galaxies with SFRs below $\approx$0.3 $m_\odot$ yr^{-1} kpc^{-2} (or equivalently cold gas surface densities <300 $m_\odot$ pc^{-2}). These systems have the majority of their molecular gas concentrated in the inner regions of their host galaxy where the rotation curve is still rising, and shear is high.

A local dynamical SF relation (taking into account the local free-fall time within the galaxy disc) reproduces well our observations. Using this relation one can obtain a single SF relation, that fits ETGs, Galactic clouds and spiral/starburst galaxies at all redshifts. Despite this, the residuals around the dynamical SF relation still correlate with galaxy properties such as the shape of the potential in the inner regions. We postulate that the dynamical stability of the gas may be an important second parameter, that suppresses SF and causes much of the scatter around the best-fitting dynamical SF relation.

We discussed various mechanisms that can cause this effect, and more generally the difficulties inherent in estimating SFRs and molecular gas masses in these ETGs. A changing X_{CO} factor could potentially cause the low SFE we observe, but it cannot explain why the SFE in our study depends so strongly on dynamical quantities.

It is clear that further study will be required to fully determine the cause of the low SFE in ETGs. Ascertaining what is driving the residuals around the KS and KDM12 law will give us a direct way to probe the physics that regulates SF. For instance, if variations in cloud properties and gas velocity dispersions are present in the central parts of ETGs, then they can potentially explain some of the SFE trends. Obtaining observational evidence for such variations will require high angular and spectral resolution observations, to resolve individual molecular clouds. Gas-phase metallicity estimates and observations of multiple spectral lines could also be used to determine if the X_{CO} factor in these objects is systematically different. In addition, studies of the stability of the gas, and comparison with spatially resolved SF relations, will be crucial to determine how changes in galactic conditions affect the physics of SF.

ACKNOWLEDGEMENTS

The research leading to these results has received funding from the European Community's Seventh Framework Programme (/FP7/2007-2013/) under grant agreement no. 229517. MC acknowledges support from a Royal Society University Research Fellowship. This work was supported by the rolling grants Astrophysics at Oxford PP/E001114/1 and ST/H002456/1 and visitors grants PPA/V/S/2002/00553, PP/E001564/1 and ST/H504862/1 from the UK Research Councils. RLD acknowledges travel and computer grants from Christ Church, Oxford and support from the Royal Society in the form of a Wolfson Merit Award 502011.K502/jd. RLD is also grateful for support from the Australian Astronomical Observatory Distinguished Visitors programme, the ARC Centre of Excellence for All Sky Astrophysics, and the University of Sydney during a sabbatical visit. SK acknowledges support from the Royal Society Joint Projects grant JP0869822. RMMD is supported by the Gemini Observatory, which is operated by the Association of Universities for Research in Astronomy, Inc., on behalf of the international Gemini partnership of Argentina, Australia, Brazil, Canada, Chile, UK, and USA. TN and MBois acknowledge support from the DFG Cluster of Excellence 'Origin and Structure of the Universe'. MS acknowledges support from a STFC Advanced Fellowship ST/F009186/1. PS is a NWO/Veni fellow. MBois has received, during this research, funding from the European Research Council under the Advanced Grant Programme no. 267399-Momentum. LMY acknowledges support from NSF grant AST-1109803. The authors acknowledge financial support from ESO.

This paper is based on observations carried out with the IRAM 30 m Telescope and the CARMA interferometer. IRAM is supported by INSU/CNRS (France), MPG (Germany) and IGN (Spain). Support for CARMA construction was derived from the states of California, Illinois, and Maryland, the James S. McDonnell Foundation, the Gordon and Betty Moore Foundation, the Kenneth T. and Eileen L. Norris Foundation, the University of Chicago, the Associates of the California Institute of Technology, and the National Science Foundation. Ongoing CARMA development and operations are supported by the National Science Foundation under a cooperative agreement, and by the CARMA partner universities. This publication also makes use of data products from the *Wide-field Infrared Survey Explorer*, which is a joint project of the University of California, Los Angeles, and the Jet Propulsion Laboratory/California Institute of Technology, funded by the National Aeronautics and Space Administration.

REFERENCES

Agius N. K. et al., 2013, MNRAS, 431, 1929
Alatalo K. et al., 2011, ApJ, 735, 88

Alatalo K. et al., 2013, MNRAS, 432, 1796 (Paper XVIII)
Athey A., Bregman J., Bregman J., Temi P., Sauvage M., 2002, ApJ, 571, 272
Bayet E. et al., 2013, MNRAS, 432, 1742
Becker R. H., White R. L., Helfand D. J., 1995, ApJ, 450, 559
Bell E. F. et al., 2012, ApJ, 753, 167
Bigiel F., Leroy A., Walter F., Brinks E., de Blok W. J. G., Madore B., Thornley M. D., 2008, AJ, 136, 2846 (B08)
Binney J., Merrifield M., 1998, Galactic Astronomy/James Binney and Michael Merrifield. Princeton Univ. Press, Princeton, NJ
Bolatto A. D., Leroy A. K., Rosolowsky E., Walter F., Blitz L., 2008, ApJ, 686, 948
Bolatto A. D., Wolfire M., Leroy A. K., 2013, ARA&A, 51, 207
Bottinelli L., Gouguenheim L., 1977, A&A, 54, 641
Boyer M. L. et al., 2012, ApJ, 748, 40
Bureau M. et al., 2011, MNRAS, 414, 1887
Caldu-Primo A., Schruba A., Walter F., Leroy A., Sandstrom K., de Blok W. J. G., Ianjamasimanana R., Mogotsi K. M., 2013, AJ, 146, 150
Calzetti D. et al., 2007, ApJ, 666, 870
Cappellari M. et al., 2011a, MNRAS, 413, 813 (Paper I)
Cappellari M. et al., 2011b, MNRAS, 416, 1680
Cappellari M. et al., 2012, Nature, 484, 485
Cappellari M. et al., 2013a, MNRAS, 432, 1709 (Paper XV)
Cappellari M. et al., 2013b, MNRAS, 432, 1862 (Paper XX)
Ciesla L. et al., 2014, preprint (arXiv:1402.3597)
Clemens M. S. et al., 2010, A&A, 518, L50
Colbert J. W., Mulchaey J. S., Zabludoff A. I., 2001, AJ, 121, 808
Combes F., Young L. M., Bureau M., 2007, MNRAS, 377, 1795
Crocker A. F., Bureau M., Young L. M., Combes F., 2011, MNRAS, 410, 1197
Crocker A. et al., 2012, MNRAS, 421, 1298
Daddi E. et al., 2010, ApJ, 714, L118 (D10)
Davis T. A. et al., 2011a, MNRAS, 414, 968
Davis T. A. et al., 2011b, MNRAS, 417, 882 (Paper X)
Davis T. A. et al., 2012, MNRAS, 426, 1574
Davis T. A. et al., 2013a, MNRAS, 429, 534 (Paper XIV)
Davis T. A., Bayet E., Crocker A., Topal S., Bureau M., 2013b, MNRAS, 433, 1659
Davis T. A., Bureau M., Cappellari M., Sarzi M., Blitz L., 2013c, Nature, 494, 328
de Zeeuw P. T. et al., 2002, MNRAS, 329, 513
di Serego Alighieri S. et al., 2007, A&A, 474, 851
Dib S., Helou G., Moore T. J. T., Urquhart J. S., Dariush A., 2012, ApJ, 758, 125
Dickman R. L., Snell R. L., Schloerb F. P., 1986, ApJ, 309, 326
Downes D., Solomon P. M., 1998, ApJ, 507, 615
Elmegreen B. G., 1997, Rev. Mex. Astron. Astrofis. Ser. Conf., 6, 165
Emsellem E. et al., 2011, MNRAS, 414, 888
Ferrarotti A. S., Gail H. P., 2006, A&A, 447, 553
Genzel R. et al., 2010, MNRAS, 407, 2091 (G10)
Genzel R. et al., 2012, ApJ, 746, 69
Gil de Paz A. et al., 2007, ApJS, 173, 185
Grossi M. et al., 2009, A&A, 498, 407
Hao C.-N., Kennicutt R. C., Johnson B. D., Calzetti D., Dale D. A., Moustakas J., 2011, ApJ, 741, 124
Herwig F., 2005, ARA&A, 43, 435
Hinz J. L., Rieke G. H., 2006, ApJ, 646, 872
Hirashita H., 2010, MNRAS, 407, L49
Jarrett T. H., Chester T., Cutri R., Schneider S., Skrutskie M., Huchra J. P., 2000, AJ, 119, 2498
Kaviraj S. et al., 2007, ApJS, 173, 619
Kennicutt R. C., 1998, ApJ, 498, 541 (K98)
Knapp G. R., Turner E. L., Cunniffe P. E., 1985, AJ, 90, 454
Knapp G. R., Guhathakurta P., Kim D.-W., Jura M. A., 1989, ApJS, 70, 329
Krajnović D. et al., 2011, MNRAS, 414, 2923
Krips M., Crocker A. F., Bureau M., Combes F., Young L. M., 2010, MNRAS, 407, 2261
Kron R. G., 1980, ApJS, 43, 305
Kroupa P., 2001, MNRAS, 322, 231
Kruijssen J. M. D., Longmore S. N., Elmegreen B. G., Murray N., Bally J., Testi L., Kennicutt R. C. J., 2013, preprint (arXiv:1303.6286)
Krumholz M. R., Dekel A., McKee C. F., 2012, ApJ, 745, 69 (KDM12)
Leroy A. K. et al., 2011, ApJ, 737, 12
Leroy A. K. et al., 2013, AJ, 146, 19
Longmore S. N. et al., 2013, MNRAS, 429, 987
Martig M., Bournaud F., Teyssier R., Dekel A., 2009, ApJ, 707, 250
Martig M. et al., 2013, MNRAS, 432, 1914 (Paper XXII)
Mathews W. G., Temi P., Brighenti F., Amblard A., 2013, ApJ, 768, 28
Matsuura M. et al., 2011, Science, 333, 1258
Meidt S. E. et al., 2013, ApJ, 779, 45
Meier D. S., Turner J. L., Beck S. C., Gorjian V., Tsai C.-W., Van Dyk S. D., 2010, AJ, 140, 1294
Momose R. et al., 2013, ApJ, 772, L13
Morganti R. et al., 2006, MNRAS, 371, 157
Oka T., Hasegawa T., Hayashi M., Handa T., Sakamoto S., 1998, ApJ, 493, 730
Oosterloo T. et al., 2010, MNRAS, 409, 500
Regan M. W., Thornley M. D., Helfer T. T., Sheth K., Wong T., Vogel S. N., Blitz L., Bock D. C.-J., 2001, ApJ, 561, 218
Rujopakarn W. et al., 2010, ApJ, 718, 1171
Saintonge A. et al., 2011, MNRAS, 415, 61
Saintonge A. et al., 2012, ApJ, 758, 73
Salim S., Rich R. M., 2010, ApJ, 714, L290
Sandstrom K. M. et al., 2012, ApJ, 777, 5
Sarzi M. et al., 2010, MNRAS, 402, 2187
Sarzi M. et al., 2013, MNRAS, 432, 1845
Schlegel D. J., Finkbeiner D. P., Davis M., 1998, ApJ, 500, 525
Schmidt M., 1959, ApJ, 129, 243
Seigar M. S., 2005, MNRAS, 361, L20
Sellgren K., 1984, ApJ, 277, 623
Serra P. et al., 2012, MNRAS, 422, 1835 (Paper XIII)
Shapiro K. L. et al., 2010, MNRAS, 402, 2140
Shi F., Kong X., Wicker J., Chen Y., Gong Z.-Q., Fan D.-X., 2012, J. Astrophys. Astron., 33, 213
Silk J., 1997, ApJ, 481, 703
Skrutskie M. F. et al., 2006, AJ, 131, 1163
Smith M. W. L. et al., 2012, ApJ, 748, 123
Solomon P. M., Downes D., Radford S. J. E., Barrett J. W., 1997, ApJ, 478, 144
Tacconi L. J. et al., 2008, ApJ, 680, 246
Temi P., Brighenti F., Mathews W. G., 2005, ApJ, 635, L25
Temi P., Brighenti F., Mathews W. G., 2009, ApJ, 695, 1 (T09)
Toomre A., 1964, ApJ, 139, 1217
van Dokkum P. G., Conroy C., 2010, Nature, 468, 940
Wei L. H., Vogel S. N., Kannappan S. J., Baker A. J., Stark D. V., Laine S., 2010, ApJ, 725, L62
Welch G. A., Sage L. J., Young L. M., 2010, ApJ, 725, 100
Wilson C. D., 1995, ApJ, 448, L97
Wong T., Blitz L., 2002, ApJ, 569, 157
Wright E. L. et al., 2010, AJ, 140, 1868
Wu H., Cao C., Hao C.-N., Liu F.-S., Wang J.-L., Xia X.-Y., Deng Z.-G., Young C. K.-S., 2005, ApJ, 632, L79
Yi S. K., 2008, in Heber U., Jeffery C. S., Napiwotzki R., eds, ASP Conf. Ser. Vol. 392, Hot Subdwarf Stars and Related Objects. Astron. Soc. Pac., San Francisco, p. 3
Yi S. K. et al., 2005, ApJ, 619, L111
Young J. S., Scoville N. Z., 1991, ARA&A, 29, 581
Young J. S., Allen L., Kenney J. D. P., Lesser A., Rownd B., 1996, AJ, 112, 1903
Young L. M. et al., 2011, MNRAS, 414, 940 (Paper IV)

APPENDIX A: PASSIVE SAMPLE

Table A1. Properties of the CO non-detected ETG sample used in this work.

Galaxy	L_{K_s} $\log(L_\odot)$	$L_{22\,\mu m,obs}$ $\log(\mathrm{ergs\ s^{-1}})$	Outlier
(1)	(2)	(3)	(4)
IC0560	10.15	41.39	x
IC0598	10.35	41.27	x
IC3631	10.12	40.90	–
NGC 0448	10.52	40.93	–
NGC 0474	10.88	41.05	–
NGC 0502	10.53	40.77	–
NGC 0516	10.20	40.62	–
NGC 0525	10.06	40.81	–
NGC 0661	10.59	40.93	–
NGC 0680	10.98	41.37	–
NGC 0821	10.91	41.34	–
NGC 0936	11.25	41.66	–
NGC 1023	10.92	41.36	–
NGC 1121	10.39	40.63	–
NGC 1248	10.47	40.99	–
NGC 1289	10.70	41.28	–
NGC 2481	10.66	41.40	–
NGC 2549	10.28	40.91	–
NGC 2577	10.68	41.32	–
NGC 2592	10.46	40.76	–
NGC 2679	10.44	41.00	–
NGC 2695	10.77	41.11	–
NGC 2698	10.64	41.15	–
NGC 2699	10.40	40.80	–
NGC 2778	10.20	40.58	–
NGC 2852	10.18	40.61	–
NGC 2859	10.96	41.32	–
NGC 2880	10.50	40.70	–
NGC 2950	10.48	41.01	–
NGC 2962	10.92	41.60	–
NGC 2974	10.76	41.83	x
NGC 3098	10.40	40.99	–
NGC 3193	11.16	41.39	–
NGC 3226	10.61	41.45	x
NGC 3230	10.98	41.39	–
NGC 3248	10.28	40.36	–
NGC 3301	10.62	41.54	x
NGC 3377	10.42	40.90	–
NGC 3379	10.83	41.17	–
NGC 3384	10.72	41.06	–
NGC 3412	10.33	40.48	–
NGC 3414	10.90	41.48	–
NGC 3457	10.07	40.42	–
NGC 3458	10.56	40.95	–
NGC 3499	10.06	40.90	x
NGC 3530	10.11	40.62	–
NGC 3605	10.04	40.52	–
NGC 3608	10.77	40.99	–
NGC 3610	10.79	41.28	–
NGC 3613	11.02	41.06	–
NGC 3630	10.58	40.96	–
NGC 3640	11.15	41.73	–
NGC 3641	10.05	40.38	–
NGC 3648	10.54	41.03	–
NGC 3658	10.69	41.46	–
NGC 3674	10.60	40.80	–
NGC 3694	10.25	41.90	x
NGC 3757	10.17	40.38	–

Table A1 – *continued*

Galaxy	L_{K_s} $\log(L_\odot)$	$L_{22\,\mu m,obs}$ $\log(\mathrm{ergs\ s^{-1}})$	Outlier
(1)	(2)	(3)	(4)
NGC 3796	10.05	40.68	–
NGC 3941	10.54	41.02	–
NGC 3945	11.04	41.53	–
NGC 3998	10.64	41.74	x
NGC 4026	10.52	40.94	–
NGC 4078	10.51	41.18	–
NGC 4143	10.55	41.27	–
NGC 4168	10.92	41.41	–
NGC 4179	10.58	40.68	–
NGC 4191	10.55	41.06	–
NGC 4215	10.68	41.06	–
NGC 4233	10.86	41.49	–
NGC 4251	10.78	41.36	–
NGC 4255	10.51	40.88	–
NGC 4261	11.38	42.01	–
NGC 4262	10.35	40.71	–
NGC 4264	10.51	40.96	–
NGC 4267	10.58	40.64	–
NGC 4278	10.83	41.38	–
NGC 4281	10.92	41.82	x
NGC 4339	10.31	40.35	–
NGC 4340	10.52	40.87	–
NGC 4342	10.14	40.54	–
NGC 4346	10.33	40.77	–
NGC 4350	10.56	41.13	–
NGC 4365	11.40	41.49	–
NGC 4371	10.69	41.18	–
NGC 4374	11.36	41.81	–
NGC 4377	10.28	41.26	x
NGC 4379	10.21	40.52	–
NGC 4382	11.36	41.78	–
NGC 4387	10.16	40.51	–
NGC 4406	11.33	41.73	–
NGC 4417	10.46	41.03	–
NGC 4434	10.33	40.80	–
NGC 4442	10.76	41.29	–
NGC 4458	10.02	40.26	–
NGC 4461	10.54	40.77	–
NGC 4472	11.62	41.85	–
NGC 4473	10.82	41.15	–
NGC 4474	10.22	40.87	–
NGC 4478	10.43	40.90	–
NGC 4483	10.05	40.37	–
NGC 4486	11.46	42.07	–
NGC 4486A	10.04	40.55	–
NGC 4489	9.95	40.13	–
NGC 4494	10.96	41.31	–
NGC 4503	10.60	40.90	–
NGC 4521	10.88	41.55	–
NGC 4528	10.13	40.14	–
NGC 4546	10.63	41.25	–
NGC 4550	10.22	40.60	–
NGC 4551	10.18	40.35	–
NGC 4552	11.03	41.37	–
NGC 4564	10.54	41.19	–
NGC 4570	10.70	41.35	–
NGC 4578	10.38	41.01	–
NGC 4608	10.49	41.00	–
NGC 4612	10.33	40.67	–
NGC 4621	10.97	41.29	–
NGC 4623	10.01	40.87	x
NGC 4624	10.78	40.54	–

Table A1 – *continued*

Galaxy	L_{K_s} log($L_\odot$)	$L_{22\,\mu m,obs}$ log(ergs s^{-1})	Outlier
(1)	(2)	(3)	(4)
NGC 4636	11.06	41.65	–
NGC 4638	10.52	40.87	–
NGC 4649	11.50	42.38	x
NGC 4660	10.39	40.92	–
NGC 4690	10.50	41.12	–
NGC 4697	10.88	41.20	–
NGC 4754	10.77	41.18	–
NGC 4762	11.10	41.79	–
NGC 4803	10.22	40.71	–
NGC 5103	10.26	40.77	–
NGC 5198	10.95	41.24	–
NGC 5308	10.96	41.09	–
NGC 5322	11.42	41.96	–
NGC 5353	11.36	41.96	–
NGC 5355	10.27	41.15	x
NGC 5422	10.79	41.06	–
NGC 5473	11.01	41.52	–
NGC 5475	10.46	41.19	–
NGC 5485	10.76	41.36	–
NGC 5493	11.11	41.49	–
NGC 5500	10.08	40.57	–
NGC 5507	10.59	40.97	–
NGC 5557	11.26	41.49	–
NGC 5574	10.23	40.95	–
NGC 5576	10.97	41.17	–
NGC 5582	10.62	40.97	–
NGC 5611	10.19	40.55	–
NGC 5631	10.79	41.47	–
NGC 5638	10.83	41.24	–
NGC 5687	10.60	41.03	–
NGC 5770	10.17	40.50	–
NGC 5813	11.35	41.79	–
NGC 5831	10.79	41.12	–
NGC 5838	10.96	41.65	–
NGC 5839	10.32	40.68	–

Table A1 – *continued*

Galaxy	L_{K_s} log($L_\odot$)	$L_{22\,\mu m,obs}$ log(ergs s^{-1})	Outlier
(1)	(2)	(3)	(4)
NGC 5845	10.48	40.99	–
NGC 5846	11.32	41.58	–
NGC 5854	10.63	41.25	–
NGC 5864	10.76	41.18	–
NGC 5869	10.62	40.97	–
NGC 6010	10.72	41.23	–
NGC 6017	10.32	41.44	x
NGC 6149	10.35	41.02	–
NGC 6278	10.99	41.43	–
NGC 6547	10.75	41.03	–
NGC 6548	10.59	42.04	x
NGC 6703	10.85	41.23	–
NGC 7280	10.44	40.98	–
NGC 7332	10.81	41.38	–
NGC 7457	10.26	40.68	–
PGC016060	10.37	41.73	x
PGC042549	10.40	41.36	x
PGC051753	10.08	40.53	–
PGC054452	9.95	40.31	–
UGC04551	10.48	40.54	–
UGC06062	10.44	41.12	–

Notes. Column one lists the name of the galaxy. Column 2 contains the K_s band luminosity of the galaxy, calculated using the 2MASS total K_s-band magnitude and the distance to these objects as in Paper I, and assuming that the absolute magnitude of the Sun at K_s-band is 3.28 mag (Binney & Merrifield 1998). Column 3 contains the *WISE* 22 μm luminosity of the galaxy, calculated as described in Section 2, once again using the distances from Paper I. Column 4 lists galaxies that were flagged as outliers in our survival analysis fit (marked with an 'x'). These objects are likely to have a molecular ISM and SF but were not detected in CO, probably due to the fixed flux limit of our survey.

APPENDIX B: CONSTANT STAR FORMATION EFFICIENCY STAR-FORMATION RELATIONS

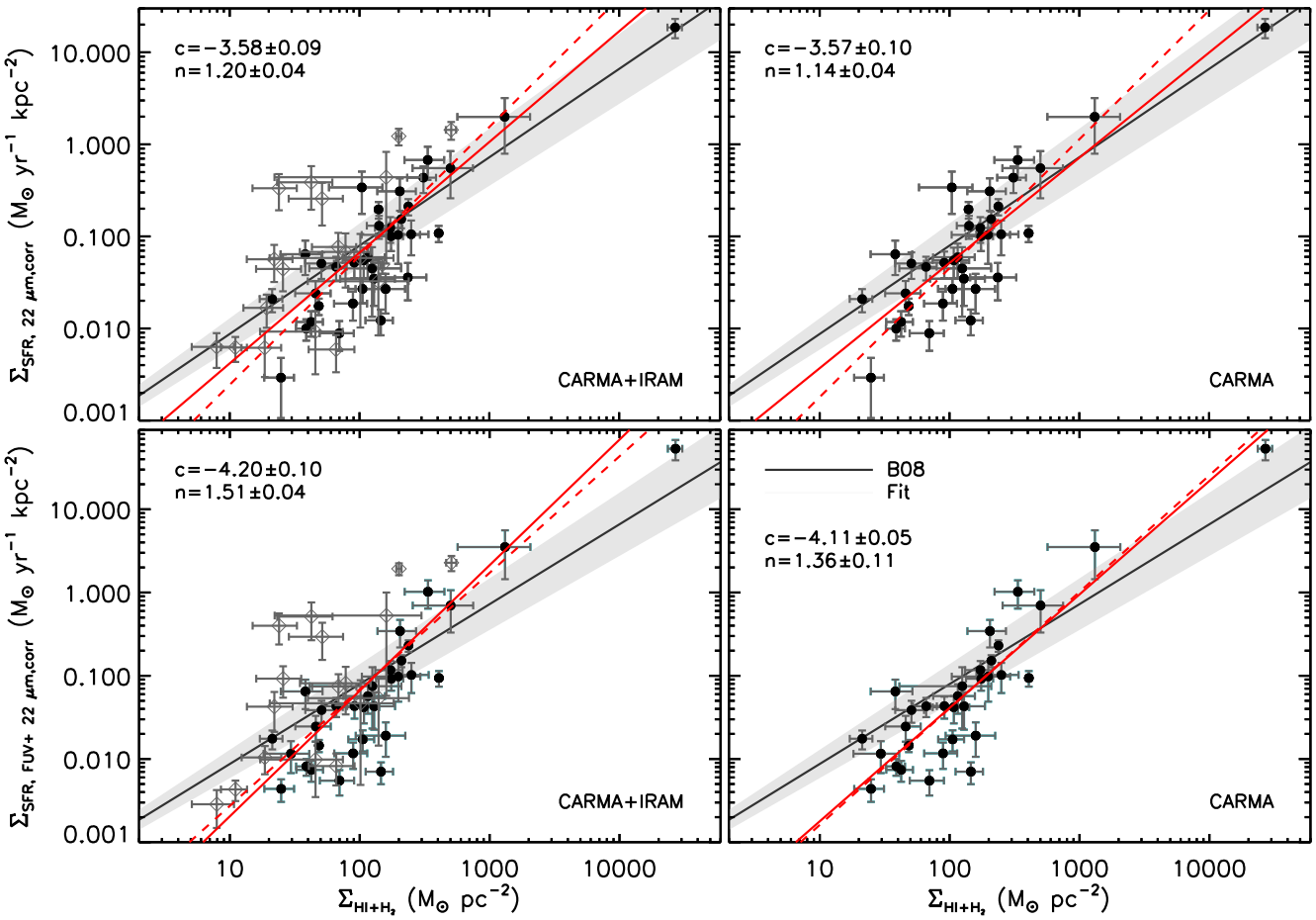

Figure B1. As Fig. 4, but showing the constant SFE relation of B08 as a black line, and its typical scatter as the grey shaded area.

APPENDIX C: RESIDUALS AROUND DYNAMICAL STAR-FORMATION RELATIONS

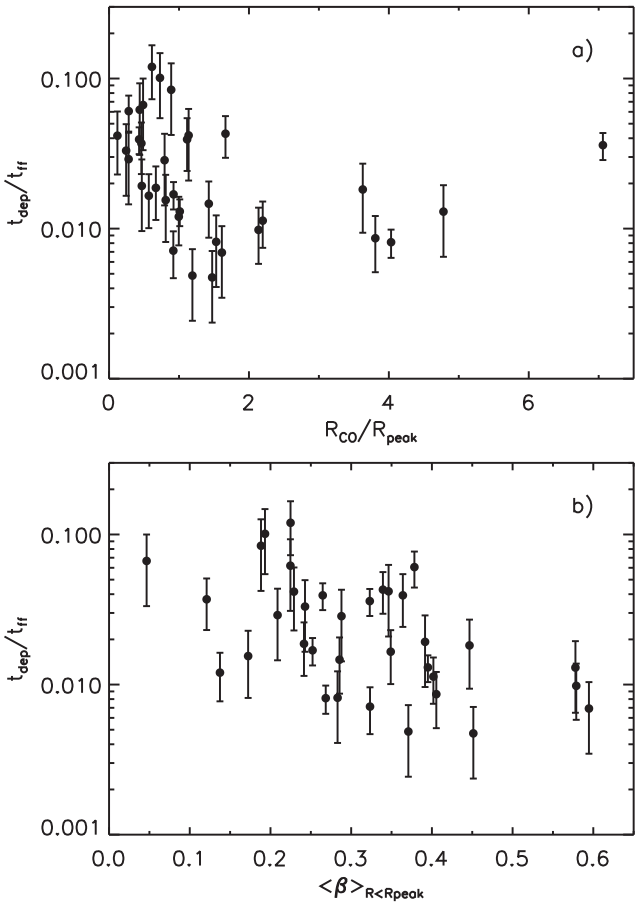

Figure C1. As in Fig. 8 (panels a and c), but with gas depletion times normalized by the local free-fall time, calculated as described in KDM12. This shows that residual dependences on galaxy dynamics remain when normalizing by the free-fall time alone.

[1]*European Southern Observatory, Karl-Schwarzschild-Str. 2, D-85748 Garching, Germany*
[2]*Physics Department, New Mexico Institute of Mining and Technology, Socorro, NM 87801, USA*
[3]*Academia Sinica Institute of Astronomy & Astrophysics, PO Box 23-141, Taipei 10617, Taiwan, R.O.C.*
[4]*Ritter Astrophysical Observatory, University of Toledo, Toledo, OH 43606, USA*
[5]*Sub-Department of Astrophysics, Department of Physics, University of Oxford, Denys Wilkinson Building, Keble Road, Oxford OX1 3RH, UK*
[6]*Department of Astronomy, Campbell Hall, University of California, Berkeley, CA 94720, USA*
[7]*Infrared Processing and Analysis Center, California Institute of Technology, Pasadena, CA 91125, USA*
[8]*Université Lyon 1, Observatoire de Lyon, Centre de Recherche Astrophysique de Lyon and Ecole Normale Supérieure de Lyon, 9 avenue Charles André, F-69230 Saint-Genis Laval, France*
[9]*Max-Planck-Institut für Astrophysik, Karl-Schwarzschild-Str. 1, D-85741 Garching, Germany*
[10]*Observatoire de Paris, LERMA and CNRS, 61 Av. de l'Observatoire, F-75014 Paris, France*
[11]*Laboratoire AIM Paris-Saclay, CEA/IRFU/SAp – CNRS – Université Paris Diderot, F-91191 Gif-sur-Yvette Cedex, France*
[12]*Sterrewacht Leiden, Leiden University, Postbus 9513, NL-2300 RA Leiden, the Netherlands*
[13]*Royal Observatory Edinburgh, Blackford Hill, Edinburgh EH9 3HJ, UK*
[14]*Leibniz-Institut für Astrophysik Potsdam (AIP), An der Sternwarte 16, D-14482 Potsdam, Germany*
[15]*Space Telescope European Coordinating Facility, European Southern Observatory, Karl-Schwarzschild-Str. 2, D-85748 Garching, Germany*
[16]*Australian Astronomical Observatory, PO Box 915, North Ryde, NSW 1670, Australia*
[17]*Netherlands Institute for Radio Astronomy (ASTRON), Postbus 2, NL-7990 AA Dwingeloo, the Netherlands*
[18]*Kapteyn Astronomical Institute, University of Groningen, Postbus 800, NL-9700 AV Groningen, the Netherlands*
[19]*Centre for Astrophysics Research, University of Hertfordshire, Hatfield, Herts AL1 9AB, UK*
[20]*Sydney Institute for Astronomy (SIfA), School of Physics, The University of Sydney, NSW 2006, Australia*
[21]*CSIRO Astronomy & Space Science, PO Box 76, Epping, NSW 1710, Australia*
[22]*School of Physics and Astronomy, University of St Andrews, North Haugh, St Andrews KY16 9SS, UK*

This paper has been typeset from a TEX/LATEX file prepared by the author.